A&A 520, A8 (2010)
DOI: 10.1051/0004-6361/200912855

Astronomy & Astrophysics
Special feature

Pre-launch status of the Planck mission

Planck pre-launch status: Expected LFI polarisation capability

J. P. Leahy[1,2], M. Bersanelli[3,4], O. D'Arcangelo[5], K. Ganga[6], S. M. Leach[7,8], A. Moss[9], E. Keihänen[10], R. Keskitalo[10,11], H. Kurki-Suonio[10,11], T. Poutanen[10,11,12], M. Sandri[13], D. Scott[9], J. Tauber[14], L. Valenziano[13], F. Villa[13], A. Wilkinson[1], A. Zonca[3,4], C. Baccigalupi[7,8,15], J. Borrill[16,17], R. C. Butler[13], F. Cuttaia[13], R. J. Davis[1], M. Frailis[2], E. Francheschi[13], S. Galeotta[2], A. Gregorio[18], R. Leonardi[19], N. Mandolesi[13], M. Maris[2], P. Meinhold[19], L. Mendes[20], A. Mennella[3,4], G. Morgante[13], G. Prezeau[21], G. Rocha[21,22], L. Stringhetti[13], L. Terenzi[13], and M. Tomasi[3]

(Affiliations can be found after the references)

Received 8 July 2009 / Accepted 15 May 2010

ABSTRACT

We present a system-level description of the Low Frequency Instrument (LFI) considered as a differencing polarimeter, and evaluate its expected performance. The LFI is one of the two instruments on board the ESA *Planck* mission to study the cosmic microwave background. It consists of a set of 22 radiometers sensitive to linear polarisation, arranged in orthogonally-oriented pairs connected to 11 feed horns operating at 30, 44 and 70 GHz. In our analysis, the generic Jones and Mueller-matrix formulations for polarimetry are adapted to the special case of the LFI. Laboratory measurements of flight components are combined with optical simulations of the telescope to investigate the values and uncertainties in the system parameters affecting polarisation response. Methods of correcting residual systematic errors are also briefly discussed. The LFI has beam-integrated polarisation efficiency >99% for all detectors, with uncertainties below 0.1%. Indirect assessment of polarisation position angles suggests that uncertainties are generally less than 0.°5, and this will be checked in flight using observations of the Crab nebula. Leakage of total intensity into the polarisation signal is generally well below the thermal noise level except for bright Galactic emission, where the dominant effect is likely to be spectral-dependent terms due to bandpass mismatch between the two detectors behind each feed, contributing typically 1–3% leakage of foreground total intensity. Comparable leakage from compact features occurs due to beam mismatch, but this averages to $<5 \times 10^{-4}$ for large-scale emission. An inevitable feature of the LFI design is that the two components of the linear polarisation are recovered from elliptical beams which differ substantially in orientation. This distorts the recovered polarisation and its angular power spectrum, and several methods are being developed to correct the effect, both in the power spectrum and in the sky maps. The LFI will return a high-quality measurement of the CMB polarisation, limited mainly by thermal noise. To meet our aspiration of measuring polarisation at the 1% level, further analysis of flight and ground data is required. We are still researching the most effective techniques for correcting subtle artefacts in polarisation; in particular the correction of bandpass mismatch effects is a formidable challenge, as it requires multi-band analysis to estimate the spectral indices that control the leakage.

Key words. polarization – instrumentation: polarimeters – space vehicles: instruments – techniques: polarimetric – cosmic microwave background

1. Introduction

ESA's *Planck* mission[1] is designed to provide the ultimate measurements of the primary cosmic microwave background (CMB) temperature fluctuations, limited only by fundamental uncertainties in subtracting astrophysical foreground emission (Tauber et al. 2010a). From an early stage it was clear that *Planck* could also provide unprecedented measurements of the CMB polarisation, and its two instruments have been designed as far as possible to maximise their effectiveness as polarimeters. In particular the coherent detector technology selected for the Low Frequency Instrument (LFI) is intrinsically polarisation-sensitive (Bersanelli et al. 2010).

At the same time polarimetry is not the primary goal of the mission. The LFI therefore lacks certain features that would be expected on an instrument expressly designed for accurate measurements of weak polarisation: notably, the correlation stage that would allow complete recovery of the polarisation state received by each feed horn, and also a capability for polarisation "chopping" by rotation of the polarisation orientation of each detector on the sky (such as provided by appropriate phase switching or a rotating half-wave plate). Nevertheless, the extreme stability offered by a space platform, especially at L2, promises to allow recovery of the CMB polarisation with an accuracy limited by instrumental noise at high multipoles, ℓ, and by residual foreground contamination at low multipoles. Our confidence in this has been increased by the successful polarimetry with WMAP (Page et al. 2007; Kogut et al. 2007; Hinshaw et al. 2009), which in important respects is less optimised for polarisation than *Planck*.

The importance of CMB polarimetry is now widely appreciated (e.g. Hu & Dodelson 2002). Among the various new constraints and independent checks on cosmological models that it provides, over and above total intensity measurements, the most important is that by setting limits to *B*-mode polarisation (Zaldarriaga & Seljak 1997) we directly limit the energy scale of

[1] *Planck* (http://www.esa.int/Planck) is a project of the European Space Agency – ESA – with instruments provided by two scientific Consortia funded by ESA member states (in particular the lead countries: France and Italy) with contributions from NASA (USA), and telescope reflectors provided in a collaboration between ESA and a scientific Consortium led and funded by Denmark.

inflation, giving us a unique window on physics at $\sim 10^{16}$ GeV energies.

The strategic role of LFI polarimetry within the *Planck* mission is: (i) to constrain the steep-spectrum polarised foregrounds, dominated by Galactic synchrotron emission; and (ii) to map the sky close to the minimum of foreground contamination at 70 GHz, albeit with less sensitivity to the CMB than available from *Planck*'s High Frequency Instrument (HFI, Lamarre et al. 2010). This will provide an independent check on the HFI results with different systematic uncertainties, and a much lower level of contamination by polarised thermally-emitting dust.

Mandolesi et al. (2010) demonstrate that CMB polarisation can be detected in the power spectrum with a signal-to-noise of up to 100:1. Since the power spectrum is proportional to the sky signal squared, this sets the following overall requirements on polarisation calibration:

- global multiplicative artefacts $\ll 0.5\%$;
- errors in the instrumental polarisation angles $\ll 0.05$ rad $= 3°$;
- artefacts uncorrelated with the CMB polarisation $\ll 10\%$ of polarised intensity.

The constraint on angles arises as follows: a global angle error of δ rotates each E, B harmonic component vector (a^E_{lm}, a^B_{lm}) by an angle of 2δ. Hence for the CMB where E-modes strongly dominate, $C^{EE}_\ell = \langle |a^E_{lm}|^2 \rangle$ is reduced by $\cos^2 2\delta$, i.e. an error of $4\delta^2$, to lowest order. Random angle errors will have a smaller impact, so this is a safe upper limit.

We will demonstrate that the first two requirements are easily met by the LFI. The worst instrumental artefacts are expected to be due to various forms of leakage into the polarisation of the strong total intensity signal from our Galaxy, but over much of the sky this will not be a serious contaminant.

Stronger requirements on calibration precision are placed by the desire to produce accurate maps of foreground polarisation, especially along the Galactic plane, since we know from WMAP that this is the dominant signal at LFI frequencies and resolution. While we do not expect to recover maps which are noise-limited at all pixels, we show that measurement of polarisation to 1% of total intensity or better appears achievable, although some potential hurdles remain to be overcome.

In this paper we present a system-level overview of the LFI as a polarimeter. Section 2 reviews the standard notation of Stokes parameters and discusses the several coordinate systems used to express them in this paper. Section 3 describes the overall architecture of the system, while Sect. 4 connects this to the Jones and Mueller matrix formalisms, to allow us to build up the system-level performance from component-level measurements and models. The LFI is most generally characterised by a polarisation response Stokes vector (which depends on both frequency and sky position) for each detector. In principle this formalism provides a complete description of all multiplicative instrumental effects, and hence of all multiplicative systematic errors, which can be defined as differences between the true response and the (relatively) idealised response assumed in the data reduction.

Analyses of polarisation systematics frequently specialise this general approach to capitalise on simplifying features of the instrument: for instance, Mueller matrices may be independent of direction, in which case a perturbation analysis may be applied to isolate the dominant departures from the ideal identity matrix: for example see O'Dea et al. (2007) for the case of a rotating wave-plate. Similarly, Hu et al. (2003) give a first-order perturbation analysis of the impact on polarisation of departures of the beamshape from an ideal circular Gaussian. Partly because *Planck* is not primarily a polarimetric mission, we cannot make much use of such simplifications, although the dominant beam-dependent polarisation residuals do indeed correspond to some of the patterns discussed by Hu et al.

Section 5, therefore, presents quantitative details of the system parameters that affect the polarisation response vectors, as known prior to launch. Since LFI detectors are highly linear over the range of sky signal strengths expected on-orbit, the only other class of systematic errors are additive effects such as $1/f$ noise; in fact the suppression of such terms is the driving factor in the design of both the LFI instrument and its data analysis pipeline. Such terms are addressed in Sects. 6 and 7: Section 6 discusses additive terms due to residual instrumental temperature fluctuations, based on the cryogenic tests for LFI and *Planck*, while Sect. 7 addresses the impact of $1/f$ noise.

The effective polarisation response varies from sky pixel to sky pixel under the control of the scanning strategy, so the only way to assess the impact of residual instrumental effects on angular power spectra is through simulations of a complete sky survey. This is also done in Sect. 7, which also allows us to discuss the possibility of checking the polarisation calibration using astronomical sources. Section 8 summarises our results.

2. Stokes parameters and coordinates

It is convenient to express the polarisation state of electromagnetic radiation either via Stokes parameters $\{I, Q, U, V\}$ or, more naturally, via the linearly polarised intensity p and orientation angle Θ. We use the term "orientation" rather than direction for Θ to signify that a rotation of 180° has no physical significance, which is to say that linear polarisation is a spin-2 quantity in the sense of Zaldarriaga & Seljak (1997). The Stokes parameters can be defined in terms of the complex amplitudes E_x, E_y of the wave in the $\hat{\boldsymbol{x}}$ and $\hat{\boldsymbol{y}}$ directions ($\hat{\boldsymbol{z}}$ being the propagation direction) via:

$$I = \left\langle |E_x|^2 + |E_y|^2 \right\rangle \quad (1)$$

$$Q = \left\langle |E_x|^2 - |E_y|^2 \right\rangle = p \cos 2\Theta \quad (2)$$

$$U = 2 \left\langle \Re(E_x^* E_y) \right\rangle = p \sin 2\Theta \quad (3)$$

$$V = 2 \left\langle \Im(E_x^* E_y) \right\rangle \quad (4)$$

(e.g. Kraus 1966). Stokes I is the total intensity, irrespective of polarisation; Q and U represent linear, and V circular, polarisation. Stokes parameters (and p) may represent either flux density or intensity (brightness). In CMB analysis I is often referred to as "temperature" while Q and U are termed "polarisation", but this is misleading inasmuch as in this context *all* Stokes parameters are measured in temperature units (cf. Berkhuijsen 1975).

In the following we often use the Stokes vector $\mathcal{S} = (I, Q, U, V)^T$ (we use calligraphic script for Stokes vectors and the matrices that act on them to distinguish them from real-space vectors). For I and V this is just a notational convenience as they transform as scalars under real-space rotation; but the projection of $\mathcal{S}$ into the (Q, U) plane has a vector nature, in that its components depends on the chosen coordinate system: an angle 2Θ in (Q, U) corresponds to an orientation of Θ on the sky. To define the zero-point of Θ, we need to relate the local x and y used above, defined only for one line of sight, to a global coordinate

system. The astronomical convention[2] takes $\hat{\boldsymbol{x}}$ as due north (the local meridian) and $\hat{\boldsymbol{y}}$ along the local parallel towards the east, consistent with propagation ($\hat{\boldsymbol{z}}$) towards the observer. It is also necessary to specify which coordinate system is intended, viz. equatorial, ecliptic or galactic, and for the first two the reference equinox (e.g. J2000 or date of observation). Many analyses of CMB polarisation adopt the opposite handedness, resulting in a change of sign of U and Θ. In this paper we use the astronomical convention throughout.

To describe the instrumental polarisation properties, we also need coordinate systems fixed with respect to the instrument. *Planck* is conventionally described by a Cartesian "spacecraft" frame in which the telescope is mirror-symmetric across the $X_{\rm SC}Z_{\rm SC}$ plane, with the ray from the centre of the focal plane oriented at 85° from $\hat{\boldsymbol{X}}_{\rm SC}$ towards $\hat{\boldsymbol{Z}}_{\rm SC}$. In flight, the telescope spins at $f_{\rm spin} \approx 1$ rpm, with its spin vector nominally parallel to $\hat{\boldsymbol{X}}_{\rm SC}$ and kept close to the anti-Sun direction. Hence the detector beams scan the sky along nearly-great circles, which are most conveniently described as parallels in a coordinate frame taking the spin axis as its pole; we refer to this as the ZS frame (mnemonic that $\hat{\boldsymbol{Z}}_{\rm ZS} = \hat{\boldsymbol{X}}_{\rm SC}$ is the spin axis). We specify the polarisation orientation of the detectors, ψ, relative to the meridians of the ZS frame, and define the rotation of this orientation relative to the celestial meridian in the pointing direction as χ (Fig. 1).

Finally, the radiation pattern ("beam") of each feed horn, after folding through the telescope optics, is defined using a variant[3] of Ludwig's 3rd definition of coordinates (Ludwig 1973) rather than polar coordinates, with the origin taken as the peak of the beam and orientated so that the co-polar axis is parallel to the projected polarisation of the "side-arm" radiometer (see Sect. 3.1) at the beam peak (Sandri et al. 2010). Fortunately, the sky regions covered by the main beam patterns are small enough that we may use the flat-sky approximation when integrating the polarisation response over the main beam.

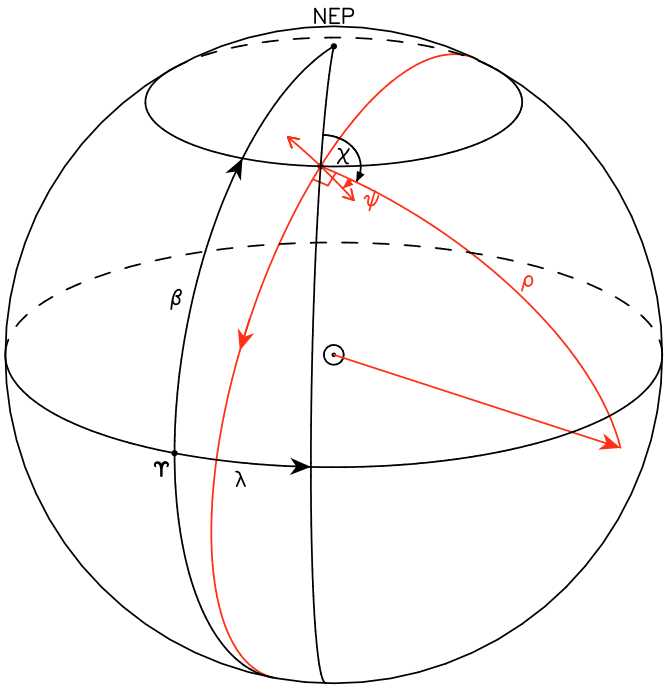

Fig. 1. Geometry of spin axis (red arrow directed away from the Sun) and scan line illustrated on a view of the celestial sphere. The north ecliptic pole is marked NEP and the vernal point, i.e. the origin of (λ, β), is marked ϒ. In black are shown the Ecliptic, the prime ecliptic meridian, and the parallel and meridian of the pixel with ecliptic longitude and latitude (λ, β). In red are shown features fixed in ZS coordinates: the scan circle, with an arrow indicating the direction the detectors scan over the sky, the scan circle radius ρ, and the polarisation orientation (double-headed arrow rotated by ψ relative to the ZS meridian). The position angle offset χ between ecliptic and ZS coordinates for the marked pixel is also shown. Note that χ and ψ are measured *anticlockwise* as seen from inside the celestial sphere.

3. LFI polarimeter architecture

3.1. Differencing polarimeter concept

The output signal power produced by a linear, narrow-band detector observing a polarised source can be written in terms of the source Stokes parameters as:

$$P = \frac{\Gamma}{2}\left(I + \Lambda(Q\cos 2\theta + U \sin 2\theta) + \xi V\right) \qquad (5)$$

(e.g. Kraus 1966). Here Γ is a gain factor, Λ is the linear polarisation efficiency ("polefficiency"), $\theta = \psi + \chi$ is the detector polarisation orientation in the coordinates used to define (Q, U), and ξ represents the response to circular polarisation. The factor of $1/2$ is included for later convenience. Note that θ gives the orientation of the detector, while Θ in Eqs. (2) and (3) is for the incoming radiation; evidently the response is $\propto \cos 2(\Theta - \theta)$. Equation (5) applies to both coherent and incoherent detectors (such as bolometers). We also have $\Lambda^2 + \xi^2 \leq 1$, with equality holding for a lossless coherent detector. Any detector comprises part of an optical system (e.g. telescope) and the detector parameters Γ, Λ, θ and ξ will be functions of frequency ν and source direction $\hat{\boldsymbol{n}}$ via the beam. In addition, they are functions of frequency but not direction due to internal components such as filters within the detector. In Sect. 4.1, we show how Eq. (5) can be computed from the Jones matrices of individual components in the receiver chain.

Table 1. Geometric parameters for the LFI focal plane.

Horn		Band	ρ^a	ϕ^b	ψ^c	
Lead	Trail				Side	Main
LFI-18	LFI-23	70 GHz	87.°20	2.°46	−22.°03	67.°67
LFI-19	LFI-22	70 GHz	87.°77	1.°55	−22.°30	67.°70
LFI-20	LFI-21	70 GHz	88.°10	0.°63	−22.°36	67.°74
LFI-24		44 GHz	89.°05	0.°00	0.°00	90.°00
LFI-26	LFI-25	44 GHz	82.°59	4.°43	−112.°52	−23.°32
LFI-28	LFI-27	30 GHz	88.°90	1.°93	−22.°20	67.°50

Notes. [(a)] Scan circle radius (ZS co-latitude); [(b)] phase along scan circle (ZS longitude); [(c)] polarisation orientation relative to ZS meridians (See Fig. 1), using the astronomical sign convention (positive from north to east). Note that the $\psi_{\rm MB}$ listed by Sandri et al. (2010) use a different geometrical definition. We only quote parameters for the leading horn in each matched pair: the values of ϕ and ψ for the trailing horn are the negatives of those quoted.

[2] As resolved by the IAU (Heeschen & Howard 1974). They specify that Stokes parameters should be defined with respect to equatorial coordinates, which is too limiting in the current context, but we prefer to avoid the confusion caused by reversing the sense of position angle. See also Hamaker & Bregman (1996).

[3] We use the convention of the GRASP software (Pontoppidan 2005) that the co-polar component is parallel to $\hat{\boldsymbol{x}}$ in the vicinity of the main beam, whereas Ludwig (1973) had it parallel to $\hat{\boldsymbol{y}}$.

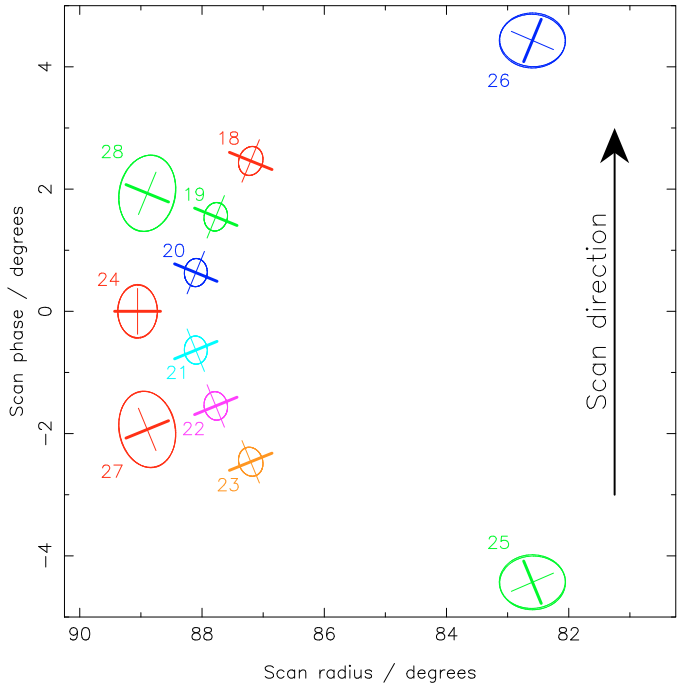

Fig. 2. Geometry of the LFI beams as projected on the sky. The ellipses show the half-maximum contour of Gaussian fits to each total intensity beam, while the crosses show the nominal polarisation orientation (heavy lines are the x or side-arm direction). Coordinates are scan circle radius ρ and scan circle phase ϕ, which correspond to co-latitude and longitude in ZS coordinates, i.e. where the spin axis gives the $\theta = 0$ direction and zero longitude is the meridian through the centre of the focal plane. The large arrow indicates the direction the beam patterns scan across the sky.

Circular polarisation is usually zero, at most a few tenths of a percent for some point sources. Moreover the LFI detectors are linearly polarised so ξ is small; in the following we will usually neglect the circular polarisation terms.

The LFI consists of eleven receiver chain assemblies (RCAs), each comprising a feed horn which couples radiation from *Planck*'s optics into an orthomode transducer (OMT) which separates it into two (nominally) orthogonal linearly polarised components along the so-called "side" and "main" OMT arms (D'Arcangelo et al. 2009b). The signal in each arm is separately amplified and detected by its own pseudo-correlation receiver, in which the radiation from the sky, via the telescope, feed, and OMT is differenced against thermal emission from a cold load at a nominal 4 K (Bersanelli et al. 2010). There is a separate 4-K load for each arm of each RCA; however, the two loads for a given RCA are located physically close together, so that drifts in the load temperature are strongly correlated between the two (Valenziano et al. 2009).

By summing and differencing the calibrated outputs of these two radiometers, this configuration allows the recovery of I and one component of the (Q, U) vector, which we denote $Q_{\rm H}$, that is, Stokes Q in the horn coordinate frame.

Initially we consider the quasi-monochromatic case and take the beam to be a delta-function measure of the sky brightness in the pointing direction. To express departures from the ideal case we write the estimated gains $\tilde{G} = \Gamma/(1+\gamma)$, $\Lambda = (1-\eta)/(1+\eta) \approx 1-2\eta$ (we call η the cross-polar leakage), $\psi_{\rm s} = \psi_0 + \delta_{\rm s}$, and $\psi_{\rm m} = \psi_0 + \delta_{\rm m} + \pi/2$, where subscripts "s" and "m" denote the side and main OMT arms. Using tildes to indicate quantities estimated from the data, the calibrated sum is

$$\begin{aligned}\tilde{I} &= P_{\rm s}/\tilde{G}_{\rm s} + P_{\rm m}/\tilde{G}_{\rm m} \qquad (6)\\ &= I\left[\frac{1+\gamma_{\rm s}}{2} + \frac{1+\gamma_{\rm m}}{2}\right] + \\ &\quad \frac{1+\gamma_{\rm s}}{2}(1-2\eta_{\rm s})\,[Q\cos 2(\theta_0+\delta_{\rm s}) + U\sin 2(\theta_0+\delta_{\rm s})] \\ &\quad - \frac{1+\gamma_{\rm m}}{2}(1-2\eta_{\rm m})\,[Q\cos 2(\theta_0+\delta_{\rm m}) + U\sin 2(\theta_0+\delta_{\rm m})] \\ &\approx (1+\bar{\gamma})I + \left(\frac{\gamma_{\rm s}-\gamma_{\rm m}}{2} - (\eta_{\rm s}-\eta_{\rm m})\right)Q_{\rm H} + (\delta_{\rm s}-\delta_{\rm m})U_{\rm H}. \qquad (7)\end{aligned}$$

The last line is a first-order approximation in the small quantities γ, η and δ. $Q_{\rm H}$ and $U_{\rm H}$ now refer to the nominal horn frame, rotated by $\theta_0 = \psi_0 + \chi$ from the sky frame, and bars indicate averages between side and main arms. Polarisation is rather weak, $\sqrt{Q^2+U^2} \sim 0.1I$, even when I represents the total intensity after subtraction of the dominant, and unpolarised, monopole and dipole terms, so the polarisation terms are effectively of second order and are usually ignored. The calibrated difference signal is

$$\begin{aligned}\tilde{Q}_{\rm H} &= P_{\rm s}/\tilde{G}_{\rm s} - P_{\rm m}/\tilde{G}_{\rm m} \qquad (8)\\ &\approx \frac{\gamma_{\rm s}-\gamma_{\rm m}}{2} I \\ &\quad + (1+\bar{\gamma})(1-2\bar{\eta})\left[Q\cos 2(\theta_0+\bar{\delta}) + U\sin 2(\theta_0+\bar{\delta})\right]. \qquad (9)\end{aligned}$$

While Eq. (9) is a first-order approximation as it stands, as long as the receiver remains linear it can be made exact by relaxing the requirements that $\bar{\gamma}$, $\bar{\eta}$, and $\bar{\delta}$ represent precisely the averages of the corresponding side- and main-arm parameters. Thus there is no need to determine these parameters for the individual detectors: it suffices to measure effective polefficiencies and angles for each feed. In particular, any failure of orthogonality ($\delta_{\rm s} \neq \delta_{\rm m}$) affects $Q_{\rm H}$ via the effective $\bar{\Lambda} = 1 - 2\bar{\eta}$ (at second order, so not apparent in Eq. (9)).

We will show that the LFI is remarkably close to an ideal polarimeter with $\eta \lesssim O\left(10^{-3}\right)$ and $\delta \lesssim O\left(10^{-2}\,\text{rad}\right)$. While the basic gain calibration is expected to be good to a few tenths of a percent at worst (Sect. 5.1), two effects can lead to relatively large gain mismatch $(\gamma_{\rm s} - \gamma_{\rm m})/2$, and hence significant "forward polconversion", i.e. contamination of the polarisation signal by total intensity[4]. This term is important because I is large compared to $Q_{\rm H}$.

The first such effect is that, due to the finite bandwidth, the calibration can only be exact for one spectral shape – in practice that of CMB fluctuations since the CMB dipole is the primary calibration source (Cappellini et al. 2003). Due to differences between the bandpasses of different detectors, including between the two arms in each RCA, this gives forward polconversion for non-CMB emission, with amplitudes of up to several percent for typical spectra. This is discussed in more detail in Sect. 5.2. The second effect is that our Γ includes the overall beam profile; hence even when the data are well-calibrated for resolved emission, differences between the beam shapes for the two polarisations will give polconversion. The relevant beam patterns are analysed in Sect. 5.4, while the impact of such non-ideal beams on the maps and power spectra, and strategies for correction, are reviewed in Sect. 7.6.

[4] This quantity is known by a variety of names, e.g. "instrumental polarisation" (Tinbergen 1996); we prefer the unambiguous terminology of Hamaker (2000).

If the detectors were not subject to systematic errors and all beamshapes were identical, the "optimal" solution for lowest random errors would weight all data by their inverse variances and determine (I, Q, U) from a least-squares analysis of all the observations of each pixel. In contrast, use of the sum and difference signal, as discussed in this section, is equivalent to using equal weights for the two detectors in each RCA. In practice, the beams from the two detectors in each RCA are very much closer in shape than the beams from different RCAs (cf. Sandri et al. 2010, and Sect. 5.4). Therefore use of the difference signal to find Q and U is preferred because forward polconversion due to beam differences is much worse for a global least-squares solution, as previously found in the analysis of data from BOOMERanG (Jones et al. 2007) and WMAP (Hinshaw et al. 2009)[5]. Use of the difference signal is also expected to ameliorate various systematics common to the two OMT arms, for instance contamination of the signal by thermal fluctuations of the RCAs and 4 K loads (cf. Sect. 6). (It has no effect on polconversion due to bandpass differences, of course).

To quantify this, we note that although the noise properties of the LFI receivers are fairly well matched, in a few RCAs the white-noise sensitivities of the two arms differ by ≈20% (Meinhold et al. 2009), which gives a 40% difference in inverse-variance weighting. Such a large difference would give significant polconversion in the final maps. On the other hand, use of the difference signal has a very minor effect on the overall noise level, the worst case being at 30 GHz where it would be ≈2% higher than optimal. In contrast, there are no strong reasons to prefer the unweighted sum signal for Stokes I, given that this only improves cancellation of "reverse polconversion", i.e. leakage of Q and U into the much stronger I.

3.2. Focal plane arrangement

Figure 2 shows the positions and orientations of the LFI beams as projected on the sky, while the same data are listed in Table 1. The polarisation angles quoted account for the slight rotation induced by the telescope optics, which explains why the side and main arm angles do not differ by exactly 90°.

The (Q, U) vector at each sky pixel is measured in two ways. The most important is that all but one of the LFI feed horns are arranged in pairs which (nominally) follow the same scan path, and whose polarisation angles differ by approximately 45°. Thus the second horn effectively measures U to the first horn's Q.

In addition, over the course of a year, each LFI horn will scan each sky pixel along at least two different scan paths, in principle allowing the recovery of polarisation from the data for a single horn (Fig. 3). In practice the angle between the scan paths is usually not large (typically 10°–20°), leading to large and anisotropic errors in (Q, U) for single-horn measurements. The exception to this rule are the "deep regions" near the ecliptic poles, where each pixel is scanned several times with a wide range of scan angles.

Horn LFI-24 has no matching partner. Consequently the 44-GHz polarisation measurements derived from all three horns will be significantly asymmetric (cf. Sect. 7.2), since for each pixel a roughly isotropic measurement of (Q, U) from LFI-25 and -26 will be combined with a measurement from LFI-24 of a single component (approximately Q in ecliptic coordinates). We emphasise that no biases are caused by such an asymmetric error distribution. It is true that an optimal arrangement of three horns would have used the available data to better effect, for instance having all horns on the same scan circle (same ρ), with polarisation angles differing by 120°, but no such arrangement was feasible given other constraints.

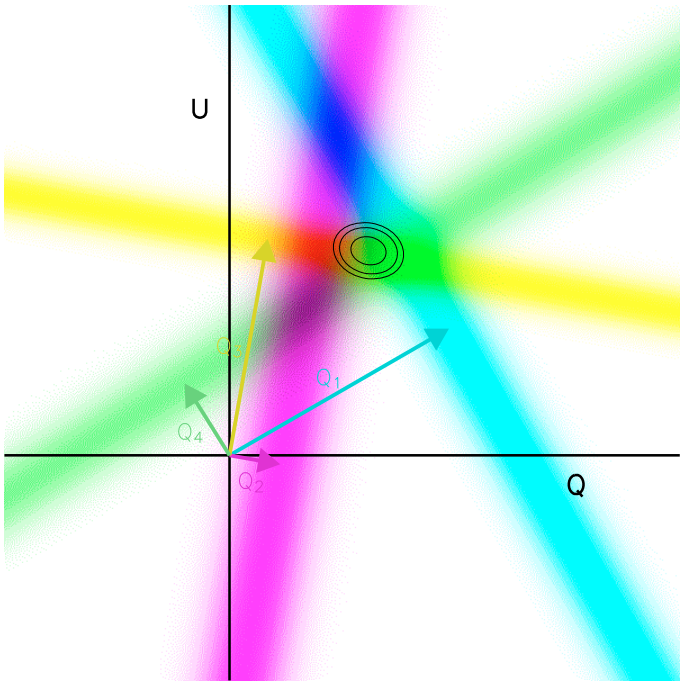

Fig. 3. Illustration of measurements in the (Q, U) plane. Each visit to the pixel by each horn measures Q_H at a different orientation, shown by the arrows Q_1, Q_2 etc., and hence constrains (Q, U) to a band in the plane (colour coded to match the relevant arrow). This schematic illustration can be considered to represent either four visits by a single horn, or two visits by a pair of horns oriented 45° apart (first pair is Q_1 [blue] & Q_4 [green], second Q_2 [purple] & Q_3 [yellow]). If the errors in each visit are Gaussian, the least-squares combined error solution is an elliptical Gaussian in (Q, U), shown as contours of χ^2, even if, as here, individual measurements are formally inconsistent with each other.

Minor asymmetries in the (Q, U) error distribution will occur in all bands due to sensitivity differences between receivers, to the fact that the pairs of horns are not oriented at exactly 45° (Table 1), and to the impact on the scan pattern of the expected slight misalignment of the spin axis. This is expected to drift relative to the satellite structure since consumption of fuel and cryogens will alter the moment of inertia. As a result, the actual scan circles for matched pairs will not be exactly identical. The spin axis misalignment from $\hat{\boldsymbol{X}}_{SC}$ is expected to be ≲5 arcmin (Tauber et al. 2010a), giving offsets between lead and trail scans of ≲0.035 $FWHM$ even in the worst case (LFI-18 and -23, the outer pair of 70 GHz horns).

The values listed in Table 1 are the nominal design values. The exact direction of the spin axis will be calibrated in flight by the star trackers, while the focal plane geometry will be calculated using observations of bright point sources, in particular planets. Hence (ρ, ϕ) will be known to sub-arcminute precision for all beams. Determination of polarisation angles ψ is more problematic. The values quoted are based on the design of the focal plane assembly (FPA), propagated using the GRASP physical optics code to the far field (Sandri et al. 2010). The GRASP code has been validated by comparison between simulations and compact array measurements of the radio frequency qualification model (RFQM) telescope (Tauber et al. 2010b). In many

[5] An alternative approach is to attempt to deconvolve the beam differences; cf. discussion in Sect. 7.6.

ways the most stringent test of the model is the approximately correct prediction of weak sidelobes of the main beam 40 dB below the peak. Since the beam is built up by synthesis, the errors all over the beam pattern should be below this level. Since the cross-polar pattern peaks at −30 to −40 dB, these results only give strong support to the co-polar pattern, but the accuracy of modelling of the cross-polar behaviour should be similar to that of the co-polar, and indeed in some cases the RFQM measurements of the cross-polar patterns match the predictions quite well. Qualitatively correct prediction of angles of polarisation response confirms that there are no gross errors, e.g. confusion of co- and cross-polar patterns. Small quantitative differences between predicted and observed polarisation are likely to be due to the imperfections of the measurement process, and the use of ideal feed-horn profiles to predict the RFQM beams (in contrast, the flight model beams discussed in this paper are based on the measured horn profiles, cf. Sandri et al. 2010).

The astrometric calibration of the focal plane geometry will allow us to correct the ψ values for shifts of the feeds or rotations of the FPA or spin axis relative to the satellite structure. It remains for us to determine any rotations of individual RCAs relative to their design orientations. This itself can be split into two parts: rotation of the physical structure of each RCA, and rotation of the true ("electrical") polarisation orientation of each detector relative to that expected from the large-scale geometry of the OMT. Neither of these angles was directly measured during the ground calibration campaign. The physical orientation is expected to be extremely close to the design value: assembly of the OMTs into the FPA was certified as compliant within the required tolerances of <50 μm and this should correspond to maximum orientation errors of less than 0.°1. The only caveat here is that the distortion of the FPA on cool-down is not well understood, with uncertainties $O(1\,\mathrm{mm})$ in the expected relative location of the FPA and the telescope focal plane at operating temperatures (Tauber et al. 2010b). The measured OMT cross-polarisation (Sect. 5.3) suggests that the electrical/mechanical misalignment is generally less than 0.°5.

Due to the lack of direct ground measurements, the polarisation angles will be checked by on-orbit observations of bright polarised sources, as discussed in Sect. 7.3.

4. Jones and Mueller matrices

In this section we generalise the monochromatic, unidirectional formalism given in Sect. 3 to finite bandwidth and beamwidth, as a preliminary to a presentation of the calibration data for the LFI.

4.1. From Jones matrix to power response

Our GRASP physical optics simulations of the beams use reciprocity, assuming that each arm of the radiometer introduces perfectly linearly polarised radiation into the base of the feed horn, with the orientation at the nominal angle. Effectively, the calculations provide a Jones matrix (e.g. Kraus 1966) for the optics, $\boldsymbol{J}^{\rm beam}(\hat{\boldsymbol{n}}, \nu)$. We follow Hamaker et al. (1996) in extending the Jones matrix notation to guided waves and electrical signals in the receiver; thus at various points in the chain the Jones vector $(E_x, E_y)^T$ represents the x and y components of a free-space wave, the waveguide modes to which these ideally couple, and the voltages resulting from their coherent detection. Departures of the OMT from ideal performance can be represented by a Jones matrix $\boldsymbol{J}^{\rm OMT}(\nu)$ which departs from the identity matrix, and the amplification stages of the radiometers can be represented by a diagonal $\boldsymbol{J}^{\rm amp}(\nu)$ since, once past the OMT, there is negligible cross-polar leakage (Davis et al. 2009). The combination is represented by the chain rule:

$$\boldsymbol{J}^{\rm total} = \begin{pmatrix} J_{xx} & J_{xy} \\ J_{yx} & J_{yy} \end{pmatrix} = \boldsymbol{J}^{\rm amp}\,\boldsymbol{J}^{\rm OMT}\,\boldsymbol{J}^{\rm beam}. \tag{10}$$

The diagonal terms are referred to as "co-polar" and the off-diagonal terms as "cross-polar". We note that the overall complex phase of any Jones matrix has no effect on the power detected; indeed, since $\boldsymbol{J}^{\rm amp}$ is diagonal, in the first two terms (from the left) we can apply an arbitrary phase to each row (Hamaker & Leahy 2004).

Equation (10) is an approximation, as it neglects reflections at interfaces between components. However, for $\boldsymbol{J}^{\rm amp}$ we will use the detailed models of the bandpass discussed by Zonca et al. (2009) and Battaglia et al. (2009), which includes all internal reflections including the interfaces between feed horn and OMT, and OMT and subsequent elements. Only missing from this are (i) terms which connect the two polarisation channels, governed by cross-polarisation (direct route) and isolation (reflected route) in the OMTs; and (ii) reflections between the feed horn and the telescope structure. For the first, cross-polarisation is assessed in the following using in the Jones matrix formalism, while measured isolation is <−40 dB across the entire band for most OMTs and <−34 dB for the rest (D'Arcangelo et al. 2009b), which justifies neglecting these terms. For the second, reflections from the telescope mirrors are essentially eliminated by the off-axis design, leaving only extremely small effects, such as scattering from telescope and baffle edges, which should also be negligible.

For a given frequency and direction Eq. (5) can be written as

$$P_i(\hat{\boldsymbol{n}}, \nu) = \mathcal{W}_i^T(\boldsymbol{R}^T(t)\,\hat{\boldsymbol{n}}, \nu)\,\mathcal{R}(\theta_0)\,\mathcal{S}(\hat{\boldsymbol{n}}, \nu), \tag{11}$$

where $\mathcal{S}$ is the Stokes vector and $\mathcal{W}_i$ is the corresponding detector response vector for detector arm i (= side, s/x, or main, m/y):

$$\mathcal{S} = \begin{pmatrix} I \\ Q \\ U \\ V \end{pmatrix}; \quad \mathcal{W}_i = \frac{1}{2}\begin{pmatrix} |J_{ix}|^2 + |J_{iy}|^2 \\ |J_{ix}|^2 - |J_{iy}|^2 \\ J_{ix}J_{iy}^* + J_{ix}^*J_{iy} \\ \mathrm{i}J_{ix}^*J_{iy} - \mathrm{i}J_{ix}J_{iy}^* \end{pmatrix}. \tag{12}$$

Note that $\mathcal{W}_i$ depends on only one row of the Jones matrix. The 3×3 rotation matrix $\boldsymbol{R}(t)$ specifies the orientation of the beam frame relative to the sky frame, while the 4×4 rotation matrix

$$\mathcal{R}(\theta_0) = \begin{pmatrix} 1 & 0 & 0 & 0 \\ 0 & \cos 2\theta_0 & \sin 2\theta_0 & 0 \\ 0 & -\sin 2\theta_0 & \cos 2\theta_0 & 0 \\ 0 & 0 & 0 & 1 \end{pmatrix} \tag{13}$$

transforms from (Q, U) defined with respect to celestial coordinates in $\mathcal{S}$ to the instrument coordinates of $\mathcal{W}$. Comparing with Eq. (5) we have

$$\mathcal{W}_{\rm s} = \frac{\Gamma_{\rm s}}{2}\begin{pmatrix} 1 \\ \Lambda_{\rm s}\cos 2\delta_{\rm s} \\ \Lambda_{\rm s}\sin 2\delta_{\rm s} \\ \xi_{\rm s} \end{pmatrix}; \quad \mathcal{W}_{\rm m} = \frac{\Gamma_{\rm m}}{2}\begin{pmatrix} 1 \\ -\Lambda_{\rm m}\cos 2\delta_{\rm m} \\ -\Lambda_{\rm m}\sin 2\delta_{\rm m} \\ \xi_{\rm m} \end{pmatrix}. \tag{14}$$

The component of the cross-polar response that is in phase with the co-polar response corresponds to an error in the nominal angle, viz

$$\delta_{\rm s}(\hat{\boldsymbol{n}}, \nu) = \frac{1}{2}\arctan\frac{2\Re(J_{xx}J_{xy}^*)}{|J_{xx}|^2 - |J_{xy}|^2} \tag{15}$$

$$\delta_{\rm m}(\hat{\boldsymbol{n}},\nu) \;=\; \frac{1}{2}\arctan\frac{-2\Re(J_{yx}J_{yy}^{*})}{|J_{yy}|^2-|J_{yx}|^2}\,, \tag{16}$$

for the side and main arms, respectively; the out of phase component gives a finite response to V. These terms are first-order in the cross-polar amplitude gain; in contrast depolarisation (finite η) is a second-order effect. At a single frequency it is due only to the loss of linearly polarised sensitivity in favour of V:

$$\Lambda_i(\hat{\boldsymbol{n}},\nu) = \sqrt{1-\xi_i^2(\hat{\boldsymbol{n}},\nu)} = \left|\frac{|J_{ix}|^2-|J_{iy}|^2}{|J_{ix}|^2+|J_{iy}|^2}\,\sec 2\delta_i\right|, \tag{17}$$

This is unity if the co- and cross-polar terms in the row, say $J_{\rm co}$ and $J_{\rm cr}$, are in phase. If they are out of phase ($\delta_i = 0$) then the cross-polar leakage $\eta_i(\nu) = |J_{\rm cr}|^2/|J_{\rm co}|^2$, which explains why η and $J_{\rm cr}$ are both sometimes called cross-polarisation; but they are distinct concepts and should not be confused. Further depolarisation occurs due to variation of δ across the band and over the beam, and also due to failure of orthogonality of the band-averaged orientations of the main and side arms (Sect. 4.3).

4.2. Mueller matrix formalism

A generic full-function polarimeter can be represented by relating the output measured Stokes vector $\tilde{\mathcal{S}}$ to the input Stokes vector via a Mueller matrix (e.g. Kraus 1966):

$$\tilde{\mathcal{S}} = \mathcal{M}\mathcal{R}(\theta_0)\,\mathcal{S}; \tag{18}$$

thus the Mueller matrix is a generalised gain. Using the notation of Eq. (11), our sum and difference signals (Eqs. (7)–(9)) can be written as

$$\tilde{I} \;=\; \left(\frac{\mathcal{W}_{\rm s}}{\tilde{G}_{\rm s}}+\frac{\mathcal{W}_{\rm m}}{\tilde{G}_{\rm m}}\right)^{T}\mathcal{R}(\theta_0)\,\mathcal{S}, \tag{19}$$

$$\tilde{Q}_{\rm H} \;=\; \left(\frac{\mathcal{W}_{\rm s}}{\tilde{G}_{\rm s}}-\frac{\mathcal{W}_{\rm m}}{\tilde{G}_{\rm m}}\right)^{T}\mathcal{R}(\theta_0)\,\mathcal{S}; \tag{20}$$

which constitute the first two lines of a Mueller-matrix equation. In the following we label Mueller-matrix elements with the Stokes parameters corresponding to the row and column (in that order); thus, for instance, $\mathcal{M}_{QI} = \mathcal{W}_{{\rm s}I}/\tilde{G}_{\rm s} - \mathcal{W}_{{\rm m}I}/\tilde{G}_{\rm m}$ controls forward polconversion.

4.3. Broad-band, beam-integrated response

All the sources detectable by the LFI are incoherent in both frequency and direction, so Eq. (11) can be integrated over frequency and solid angle to give the net power received by the detector:

$$P(t) = \int_0^\infty {\rm d}\nu \int_{4\pi} {\rm d}\Omega\; \mathcal{W}_i^T(\boldsymbol{R}^T(t)\,\hat{\boldsymbol{n}},\nu)\,\mathcal{R}(\theta_0)\,\mathcal{S}(\hat{\boldsymbol{n}},\nu), \tag{21}$$

where the Stokes vector $\mathcal{S}$ must be expressed in terms of brightness temperature (see Appendix A).

A practical drawback to this approach is that at present we do not have calculations of $\boldsymbol{J}^{\rm beam}$ at a well-sampled set of frequencies across the band (first steps towards this are discussed in Appendix B). Therefore in the following we instead evaluate separately $\mathcal{W}(\nu)$ found from $\boldsymbol{J}^{\rm amp}\boldsymbol{J}^{\rm OMT}$, and $\mathcal{W}(\hat{\boldsymbol{n}})$ evaluated from $\boldsymbol{J}^{\rm beam}$ at the nominal band frequency. A joint analysis will be the subject of a future publication.

Following the development in Appendix A it is convenient to factorise the gain $\Gamma(\nu)$ into an overall gain G, and a bandpass $g(\nu)$ normalised so that

$$\int_0^\infty g(\nu)\,\eta_{\Delta T}(\nu)\,{\rm d}\nu = \eta_{\Delta T}(\nu_0), \tag{22}$$

where $\eta_{\Delta T}(\nu)$ is the conversion factor from thermodynamic to brightness temperature for CMB fluctuations: $\Delta T_B(\nu) = \eta_{\Delta T}(\nu)\Delta T_{\rm CMB}$, and ν_0 is a fiducial frequency for the band. The bandpass shape, $g(\nu)$, is expected to be quite stable over time, whereas G is expected to drift measurably and require frequent calibration (Sect. 5.1). From the development above, we should have $\Gamma \equiv Gg = |J_{\rm co}|^2 + |J_{\rm cr}|^2$; but we neglect the cross-polar contribution as it is generally smaller than the uncertainty in the co-polar term.

5. System polarisation parameters

5.1. Receiver gain differences

Equation (9) shows that errors in the gain calibration lead directly to leakage of total intensity into the polarisation signal, so accurate gain calibration is needed to recover polarisation in the presence of much brighter total intensity. High-gain amplifiers are well known to show significant fluctuations in their gain over time, both due to stochastic fluctuations and to deterministic drifts driven by, for instance, temperature fluctuations. The latter can often be calibrated explicitly using temperature measurements recorded in the satellite telemetry, however we expect temperature-driven fluctuations to be almost negligible in the in-flight polarisation signal (see Sect. 6). The $1/f$ noise which affects such amplifiers is mainly due to gain drifts acting on the large offset signal due to the finite system temperature. Seiffert et al. (2002) and Mennella et al. (2003) estimate

$$\frac{\Delta G(f)}{G} = 2\sqrt{N_{\rm s}}Af^{\alpha/2},$$

where $N_{\rm s} \approx 10$ is the number of amplifier stages in the RCA (there are several in each of the front-end and back-end modules), $\alpha \sim -1$ is the slope of the $1/f$ noise power spectrum[6] and $A \sim 2\times10^{-5}$. The LFI design dramatically reduces this raw $1/f$ noise, driven by fractional gain errors of order 10^{-4}; and residual $1/f$ noise is effectively dealt with by our mapping algorithms (e.g. Ashdown et al. 2009). But extrapolating to long timescales, the gain drifts eventually become significant for their effect on the differential *signal* (as opposed to the $T_{\rm sys}$ offset), and need to be corrected by calibration. Specifically, on a one-hour timescale ($f \approx 0.3$ mHz), the model predicts $\Delta G/G \sim 0.7\%$, while on a 6 day timescale we get 9%. At least the latter almost certainly over-predicts the gain fluctuations: the best-monitored set of high-gain amplifiers are those on the WMAP spacecraft, and their measured gains drift by only a few percent on timescales of years; moreover the drift can be fitted by a deterministic model based on housekeeping parameters (Jarosik et al. 2007). The $1/f$ power spectrum was, after all, never intended to be extended to cover substantial gain fluctuations and these results directly confirm a low-frequency cutoff. In *Planck* also, gains are affected by the various thermal cycles and drifts on the satellite, and these will mostly be dealt with by explicit modelling using thermometric "house-keeping" data (Bersanelli et al. 2010), but any

[6] We define α as in Meinhold et al. (2009), not as in Mennella et al. (2003).

unmodelled long-timescale thermally-driven gain changes will of course be calibrated along with the stochastic $1/f$ component.

At present there are no test data runs longer than a few hours for the LFI radiometers in which they operated at nominal conditions, so the outer cutoff for LFI will be established during the on-orbit calibration phase.

Astronomical gain calibration is based on the CMB dipole, which appears as a fluctuation at the satellite spin frequency in the time-ordered data, with Rayleigh-Jeans amplitude $\eta_{\Delta T}(\nu_0)D$; this varies through the year due to geometric effects, as discussed in Sect. 7.5. If errors are dominated by noise, the 1-σ error in γ is

$$\sigma(\gamma) = \frac{\sigma_T}{\sqrt{2\tau}\,\eta_{\Delta T}(\nu_0)D}\sqrt{1+\left(\frac{f_{\rm spin}}{f_{\rm knee}}\right)^{\alpha}} \tag{23}$$

for an integration time τ and a 1-second white noise level of σ_T. The last term allows for the effect of $1/f$ noise (Meinhold et al. 2009). For reference, taking the median value, $D = 2.4$ mK, and noise parameters from Meinhold et al. (2009), we get $\sigma_\gamma = 0.56\%$, 0.41%, and 0.24% at 70, 44, and 30 GHz, respectively for a 1-h integration. The impact of residual gain errors on the maps is discussed in Sect. 7.5.

5.2. Bandpass differences

Our formalism for describing the effect of finite bandwidths on differencing polarimetry was briefly described by Leahy & Foley (2006); a more detailed presentation is in preparation. The most basic effect is to render ambiguous the operating frequency quoted for a detector: it is helpful to distinguish the *nominal frequency* used to label the band (30, 44 and 70 GHz for the LFI), the *fiducial frequency* for each band, ν_0, chosen to minimise the photometric errors to be described in this section, and the *effective frequency* for each detector, $\nu_{\rm eff}$, at which such errors are zero for a reference spectrum.

In an idealised model of gain calibration, a perfect measurement of the power due to the dipole, $P_{\rm dipole}$, gives a gain estimate of

$$\tilde{G} = \frac{2P_{\rm dipole}}{\eta_{\Delta T}(\nu_0)D} = \frac{G\int_0^\infty g(\nu)\,\eta_{\Delta T}(\nu)\,{\rm d}\nu}{\eta_{\Delta T}(\nu_0)} = G. \tag{24}$$

The corrected total intensity in Rayleigh-Jeans units for an unpolarised source with spectrum $I(\nu)$ will then be

$$\tilde{I} = \frac{2P}{\tilde{G}} = \int_0^\infty g(\nu)I(\nu)\,{\rm d}\nu \equiv \left[1+f(\beta,\nu_0)\right]\,I(\nu_0). \tag{25}$$

In general β must stand for a vector of parameters controlling the source spectral shape, but in practice a single spectral index often suffices over the 20–30% frequency range of a *Planck* bandpass. The f factor is a contribution to the band-integrated gain error γ; it is equivalent to a colour term in optical photometry. For a given source spectrum and bandpass there is an effective frequency for which f will be zero (Fig. 4); by construction it is also automatically zero when the source spectrum is $\eta_{\Delta T}$, independently of ν_0. For this reason we consider f to be an error that affects foreground emission only and write

$$\tilde{I} = \eta_{\Delta T}(\nu_0)\Delta T_{\rm CMB} + [1+f(\beta,\nu_0)]I^{\rm F}(\nu_0), \tag{26}$$

where $I^{\rm F}$ is the foreground brightness. Then β refers to the foreground emission only; we emphasise that it varies from pixel to pixel and band to band.

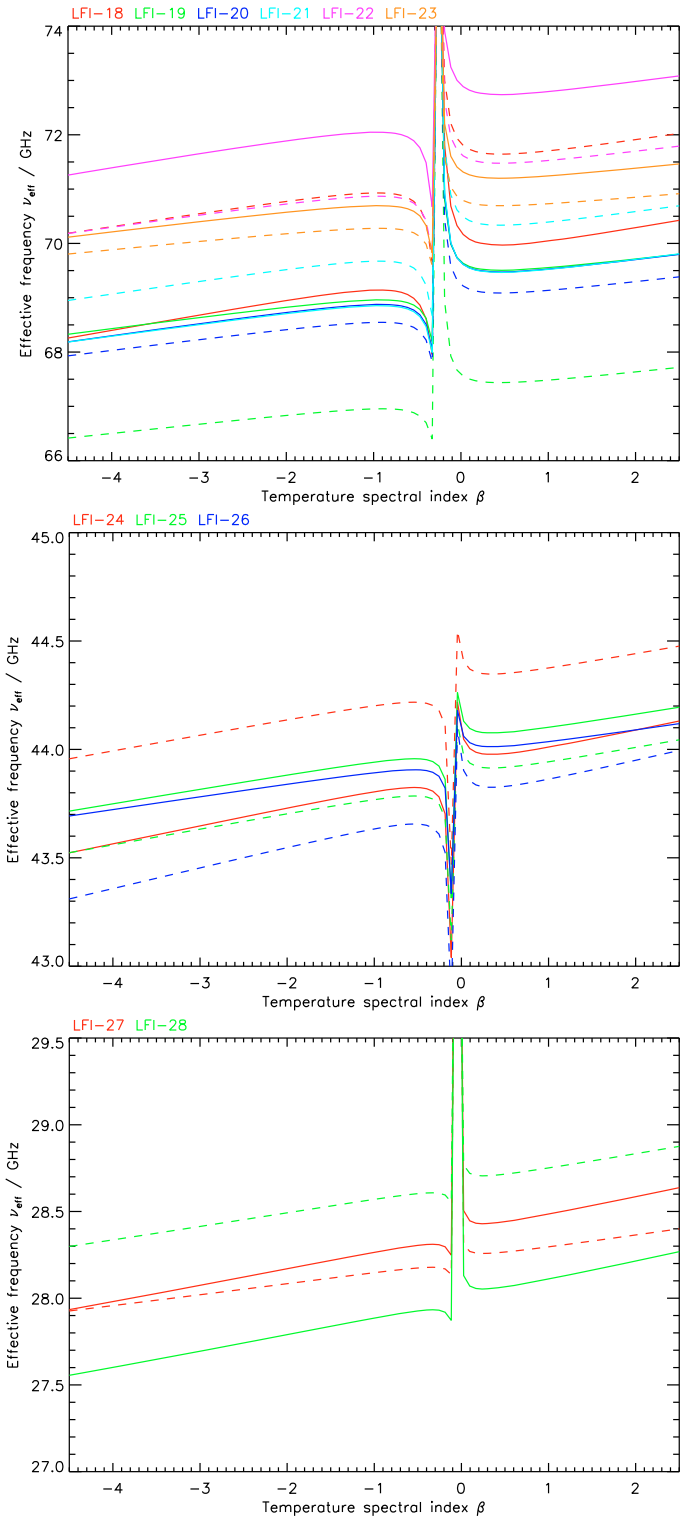

Fig. 4. Plots of effective frequency $\nu_{\rm eff}$ against spectral index β, defined by $f(\beta,\nu_{\rm eff}) = 0$, for a pure power-law sky spectrum, for each LFI detector. Solid lines are side-arm and dashed main-arm. The glitch near $\beta_{\rm CMB} \approx 0$ occurs because spectra tracking the CMB have multiple values of $\nu_{\rm eff}$, since by construction the colour term $f(\beta_{\rm CMB},\nu)$ is nearly zero for all frequencies.

We apply this formalism to the current best estimates of the LFI bandpasses, namely the QUCS models from Zonca et al. (2009). To minimise the error in the total intensity maps, we define ν_0 for each LFI band to be the mean of the individual detector $\nu_{\rm eff}$ values, when observing the dominant foreground

Table 2. Worksheet for estimating the magnitude of polconversion due to bandpass mismatch in the *Planck* frequency bands, over the full sky ("4π") and over pixels outside the WMAP KQ85 mask ("Mask").

		CMB emission		Foreground emission						Polconversion $\mathcal{M}_{QI}I^{\rm F}$	
Band	Region	$\sigma(I)^a$ (μK)	$\sigma(Q,U)^a$ (μK)	$\langle I^{\rm F}\rangle^b$ (μK)	$\langle\sqrt{Q^2+U^2}\rangle^c$ (μK)	$\langle\beta\rangle^b$	$\tilde{\beta}^{b,d}$	ν_0 (GHz)	$\sigma(\nu_{\rm eff})^e$ (GHz)	rms^f (μK)	Abs Max^f (μK)
30 GHz	4π	85	0.94	410	13	−2.89	−2.63	28.11	0.29	28.0	1300
	Mask			110	10	−2.92	−2.87			1.7	28
44 GHz	4π	89	1.31	130	4	−2.61	−2.36	43.81	0.21	4.6	210
	Mask			30	3	−2.64	−2.56			0.2	2
70 GHz	4π	89	1.91	60	3	−0.46	−0.60	69.54	1.35	1.9	140
	Mask			16	2	−0.46	−0.24			0.1	12

Notes. $\langle X\rangle$ denotes area-weighted mean values. Zonca et al. (2009) bandpasses were used to calculate ν_0, $\nu_{\rm eff}$, and $\mathcal{M}_{QI}$. $^{(a)}$ rms after convolution with the beam; $^{(b)}$ foreground temperature, $I^{\rm F}$, and spectral index, β, from the *Planck* sky model; $^{(c)}$ foreground polarisation, interpolated from WMAP; $^{(d)}$ flux-weighted mean spectral index; $^{(e)}$ standard deviation of $\nu_{\rm eff}(\tilde{\beta})$ over the detectors in each band; $^{(f)}$ rms and extreme value of the polconversion signal (mean over RCAs in each band).

spectral index in each band. The foreground properties were derived with the *Planck* sky model v1.5[7]. This is a four component model containing spinning and thermal dust, free-free and synchrotron emission. Results for mean spectral indices are given in Table 2. For our choice of nominal spectral index we use the flux weighted values, $\tilde{\beta}$, outside the WMAP KQ85 mask, except at 70 GHz, where we choose a nominal index of −0.5 because the flux weighted value is too close to the CMB spectral index, causing ambiguities in $\nu_{\rm eff}$ (cf. Fig. 4). These values of β yield $\nu_0 = 28.1$, 43.8, and 69.5 GHz, which depend only weakly on spectral index. The discrepancy in the 30 GHz band is due to the non-nominal low-frequency extension of the band revealed by Zonca et al. (2009).

The bandpasses for the main and side arms in a given RCA are determined by independent physical components (apart from the OMT itself). Moreover, due to the asymmetric design of the OMTs, the OMT contribution to the bandpass is different for the two arms. Thus the bandpasses for the two arms of a given RCA are no more similar than for any two detectors in a given band. Hence there can be significant discrepancies between main and side arm f factors, giving rise to forward polconversion, i.e. a contribution to the $\mathcal{M}_{QI}$ Mueller matrix element. Fortunately the dependence of $f(\beta,\nu_0)$ on β is very smooth, despite the considerable structure in $g(\nu)$ (Zonca et al. 2009), because of the smoothness of the source spectra. To a first approximation, the polconversion term is

$$\mathcal{M}_{QI} = \frac{f_{\rm s}-f_{\rm m}}{2} \approx (\beta-\beta_{\rm CMB})\frac{\nu_{\rm eff,s}-\nu_{\rm eff,m}}{2\nu_0}, \tag{27}$$

where $\beta_{\rm CMB}$ is the local spectral index of $\eta_{\Delta T}$:

$$\beta_{\rm CMB} = 2 - x - \frac{2x}{{\rm e}^x-1} \approx -\frac{x^2}{6}; \quad \text{with } x = \frac{h\nu_0}{k_B T_0}\cdot \tag{28}$$

Thus the artefact is dominated by the fractional difference in effective frequency between the two arms. Figure 5 shows the polconversion for each feed for power-law spectra and illustrates the quality of the approximation in Eq. (27). The apparently worst fits, for LFI-26 and LFI-27, are cases with very low polconversion, which is why second-order effects become noticeable.

A more complete parametrisation, which is generally adequate to a fraction of a percent for the LFI bandpasses, is

$$f(\beta,\beta_{\rm run},\nu_0) = f_0 + f_1\beta + f_2\beta^2 + f_{\rm run}\beta_{\rm run}. \tag{29}$$

[7] www.apc.univ-paris7.fr/APC_CS/Recherche/Adamis/PSM/psky-en.php; we used the mamd_dickinson_4comp_pred Galactic model.

where our spectral model now includes "running":

$$\ln\left(I^{\rm F}(\nu)/I^{\rm F}(\nu_0)\right) = [\beta + 0.5\beta_{\rm run}\ln(\nu/\nu_0)]\ln(\nu/\nu_0), \tag{30}$$

to give a good representation of strongly curved spectra, for example spinning dust (Draine & Lazarian 1998). The coefficients in Eq. (29) depend on ν_0, which, as noted previously, is chosen to minimise the typical correction $\langle f(\tilde{\beta},\nu_0)\rangle$.

Polconversion due to bandpass mismatch is a particularly difficult systematic to deal with, since its magnitude depends on the local foreground spectral index. It is worth keeping in mind the following relative magnitudes (cf. Table 2):

- The foreground total intensity which drives bandpass errors is weaker than the CMB fluctuations over much of the sky in all LFI bands, substantially so at 44 and 70 GHz.
- The residual error, $fI^{\rm F}$, is typically a few percent of the foreground total intensity.
- From WMAP the foregrounds are typically a few percent up to 30% polarised, with the lowest polarisation along the Galactic plane (Kogut et al. 2007). Hence the forward polconversion will be between order unity and 10% of the foreground polarisation signal.
- For $\mathcal{M}_{QI}$, corrections to the simple Eq. (27) are 1–2 orders of magnitude smaller again (Fig. 5).

We conclude that even uncorrected bandpass errors should not be a limiting factor in the ability of the *Planck* mission to separate foregrounds from CMB fluctuations in total intensity, at least to first-order accuracy in the foreground emission. To the extent that the bandpasses are known, this will allow evaluation and correction of bandpass artefacts by one or more orders of magnitude, allowing LFI to make accurate measurements of strongly-polarised foregrounds (notably the high-latitude synchrotron emission), and clear detections of polarisation where it is more than 1% of total intensity.

At present, as discussed by Zonca et al. (2009), the accuracy of our preferred QUCS bandpass models is hard to quantify. Direct measurements of the radiometer bandpasses suffered substantial errors and also had frequency ranges too restricted to clearly delineate the low-frequency cutoff of the 30 GHz band or the high-frequency cutoff of the 44 GHz band (cf. Figs. 4 and 5 of Zonca et al.). The QUCS bandpasses are simulations based on component-level measurements; however in some cases the component-level frequency range was as limited as at the radiometer level or even more so; thus the modelled 30 GHz

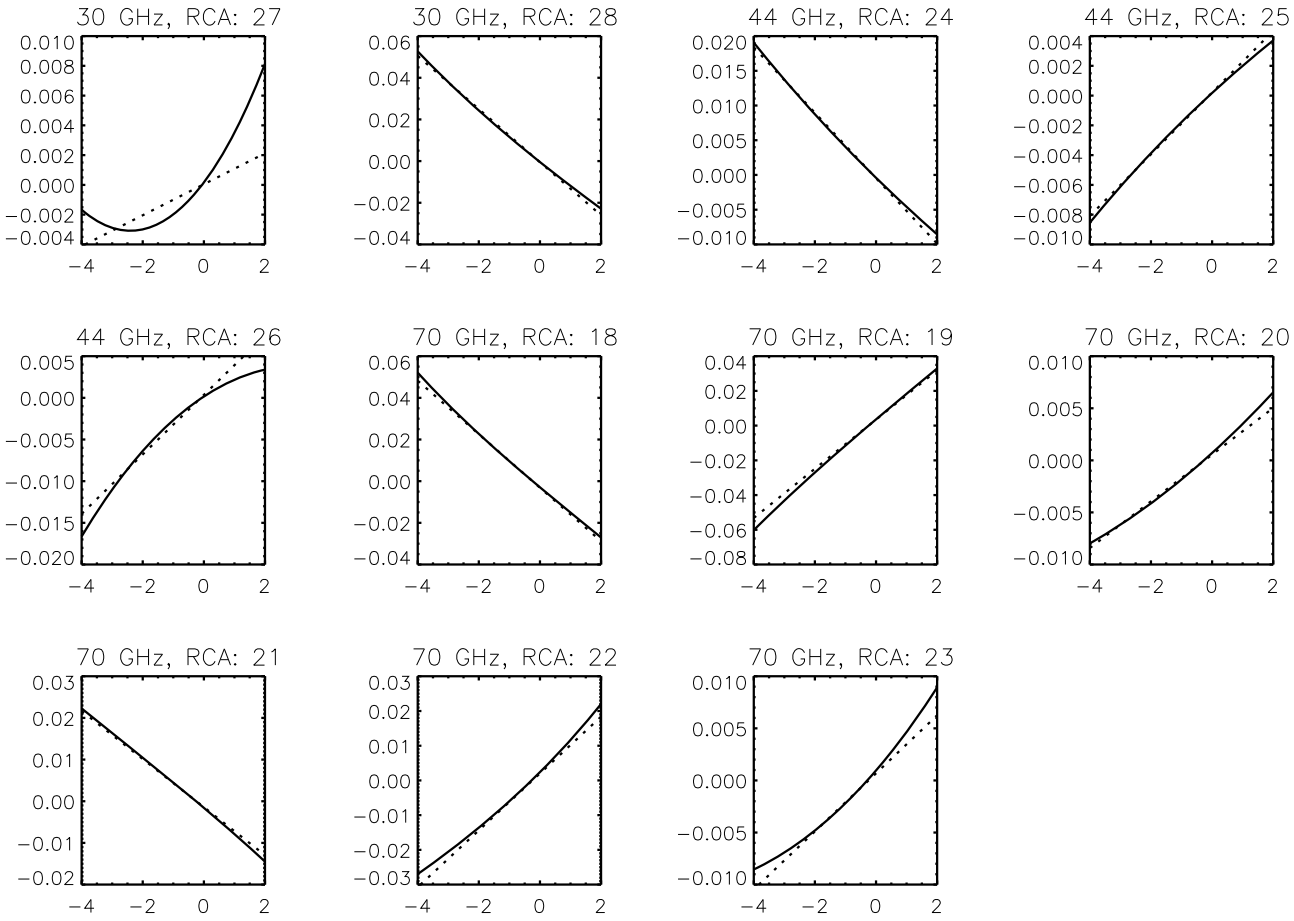

Fig. 5. Polarisation conversion term due to bandpass mismatch, $(f_s - f_m)/2$, (y-axis) for each LFI RCA, plotted against brightness-temperature spectral index β (x-axis). The dotted line shows the approximation of Eq. (27).

low-frequency cutoff depends on OMT return loss scaled from measurements of the similar 44 GHz OMTs; while the 70 GHz model barely covers the full bandpass in some cases (e.g. LFI-21, see Fig. 6), and hints at significant gain below its lower limit of 60 GHz, apparently in line with measurements (Zonca et al. Fig. 14).

We have repeated the analysis discussed above to compare the raw measurements with the QUCS models, where the effects of ill-determined band edges were removed by using only the common frequency range of measurements and models. Even so, deviation between model and measurements are large enough that the derived $f_s - f_m$ values are frequently of opposite sign. This is a difficult test to pass, since we are concerned with a second-order effect, the difference of two small terms; nevertheless we need accuracy at this level to meet our aspiration of polarisation errors below 1%. As discussed by Zonca et al. (2009), work is planned to reduce and quantify uncertainties in the QUCS models, which will include refined measurement and modelling of flight spare devices.

The flight data themselves can be used to isolate bandpass errors, by differencing total intensity maps made with different horns, and, at 70 GHz, by differencing polarisation maps made independently from the three mirror-symmetric horn pairs. In such maps bandpass errors will dominate where foreground emission is strong. This provides both a check on the predictions from the model bandpasses and, in principle, an opportunity to update bandpass parameters, in particular $\nu_{\rm eff}$, using the flight data.

5.3. Cross-polarisation response across the bandpass

The components of $\boldsymbol{J}^{\rm OMT}$ are a subset of the complex amplitudes from the scattering matrix measured in laboratory testing of the OMTs (D'Arcangelo et al. 2009b), namely

$$\boldsymbol{J}^{\rm OMT} \equiv \begin{pmatrix} \text{Side arm insertion loss} & \text{Side arm cross pol} \\ \text{Main arm cross pol} & \text{Main arm insertion loss} \end{pmatrix}. \quad (31)$$

"Insertion loss" is so named since, when measured in dB, a non-zero value represents a departure of J_{ii} from unity.

These parameters were measured for the flight model OMTs at IFP-CNR Milan, using a vector network analyser (VNA), as described by D'Arcangelo et al. (2009b). The measured phase data also included the contribution of the adaptors connecting the VNA to the OMT under test. The amplitude and phase contributions from the adaptors, essentially a linear phase gradient across the band, were measured and subtracted. Typical precision for the insertion loss signals was <0.1 dB and <1° of phase. Due to the low signal levels in the cross-polar response, repeatability was somewhat worse than for insertion loss, but analysis of four independent measurements of LFI-20 (main) showed that band-integrated results were repeatable at the level of 10^{-5} in cross-polar leakage and 0.°01 in polarisation angle.

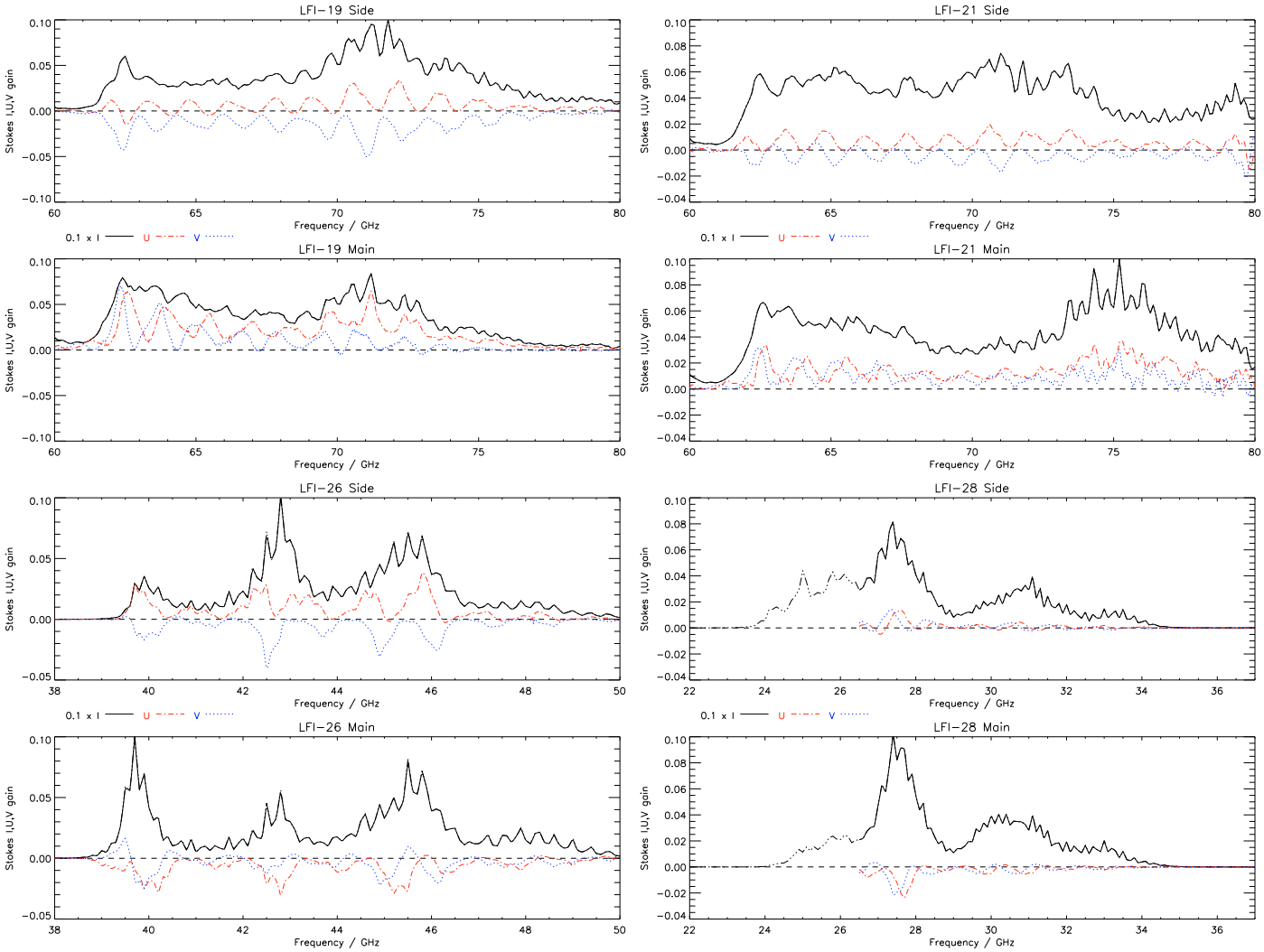

Fig. 6. Plots of the components of the detector response Stokes vector $\mathcal{W}$ against frequency, as measured for the flight model amplifiers and OMTs. In each plot the solid line shows $\mathcal{W}_I$ (i.e. the bandpass), scaled down by a factor of 10 for display purposes. On this scale $\mathcal{W}_Q$ is essentially indistinguishable from $\mathcal{W}_I$ and is not plotted. The cross-polar gains $\mathcal{W}_U$ and $\mathcal{W}_V$ are shown as dot-dashed and dotted lines, respectively. Scaling is arbitrary but self-consistent for all the curves for a given RCA. In particular the integrated CMB power for the two arms is identical, as it should be for perfect calibration. *Top left*: LFI-19 (largest η); *Top right*: LFI-21 (typical); Bottom left: LFI-26 (largest δ); *Bottom right*: LFI-28 (model bandpass extension to low frequency shown as dash-triple-dotted line).

We have derived the components of $\mathcal{W}(\nu)$ from the measured OMT and model bandpass data for each RCA arm, excluding the contribution of the optics, i.e. using $\boldsymbol{J}^{\rm amp}\,\boldsymbol{J}^{\rm OMT}$ only. For $\boldsymbol{J}^{\rm amp}$ we used the bandpass estimates of Zonca et al. (2009), but with the OMT insertion loss divided out (since this is included in $\boldsymbol{J}^{\rm OMT}$). Figure 6 plots example cases including the worst-performing OMTs.

By integrating the components of $\mathcal{W}$ over frequency we can derive band-integrated values of η and δ, which are listed in Table 3. We also give the effective $\bar{\eta}$ and $\bar{\delta}$ for the difference signal, $\tilde{Q}_{\rm H}$, assuming perfect calibration of total intensity. The integrals over the frequency band of Eq. (11) require an assumed source spectrum, and for the quoted figures we used the differential CMB spectrum, $\eta_{\Delta T}$.

As expected from the analysis in Sect. 4.1, the dominant effect is rotation of the effective angle, i.e. finite $\bar{\delta}$. The first-order prediction $\bar{\delta} \approx (\delta_{\rm s}+\delta_{\rm m})/2$ was found to be accurate for all RCAs. There is a marked tendency for a significant position-angle rotation in the main arm, of order 1°, while the side arm angles are generally much closer to nominal. The overall angle for the horn $\bar{\delta}$, only exceeds our target accuracy of 0.°5, in two cases, LFI-19 and LFI-26 (both shown in Fig. 6).

LFI-19 follows the usual pattern of a large $\delta_{\rm m}$ with a smaller $\delta_{\rm s}$ in the opposite sense. On the other hand in LFI-26, $\delta_{\rm s} \approx \delta_{\rm m}$ which suggests that a physical misalignment of the OMT during testing could have been responsible.

As a second-order effect, depolarisation is essentially negligible with all polefficiencies >99.8% and most >99.9%. The dominant source of the small depolarisation we measured is linear-to-circular conversion, with variation of δ across the band contributing almost as much in some cases. Main-vs.-side misalignment is 1°–2° for the 70 GHz OMTs, and smaller for the other bands; in all cases it a relatively minor source of depolarisation.

When observing sources with non-CMB spectra, the band integrals will be slightly different. We evaluated this effect assuming power law spectra with spectral index $\beta = -3$ (appropriate for synchrotron radiation) and $\beta = 2$ (appropriate for thermal

Table 3. Band-averaged cross-polar leakage η and effective rotation δ measured for the flight model OMTs.

Feed	Side arm		Main arm		Difference[a]	
	η_s	δ_s	η_m	δ_m	$\bar{\eta}$	$\bar{\delta}$
LFI-	10^{-3}	°	10^{-3}	°	10^{-3}	°
18	0.39	0.02	0.29	0.97	0.41	0.49
19	0.46	0.44	0.40	−1.53	0.73	−0.54
20	0.10	0.27	0.18	−0.89	0.25	−0.26
22	0.26	0.54	0.36	−1.46	0.61	−0.46
23	0.34	0.76	0.34	−1.41	0.70	−0.33
24	0.03	0.01	0.02	−0.37	0.04	−0.18
25	0.18	−0.02	0.07	−0.75	0.16	−0.39
26	0.42	0.95	0.34	0.83	0.38	0.89
27	0.02	−0.02	0.02	0.40	0.03	0.19
28	0.04	0.16	0.06	0.26	0.05	0.21

Notes. Values are weighted by the measured bandpass and the differential CMB spectrum. [(a)] effective $\bar{\eta}$ and $\bar{\delta}$ evaluated by integrating over the difference bandpasses, $\mathcal{M}_{QS} = \mathcal{W}_s(\nu)/G_s - \mathcal{W}_m(\nu)/G_m$.

dust emission), in both cases assuming that the gain calibration was determined from the CMB dipole as discussed in Sect. 5.2. We found the spectral dependence of η and δ to be negligible, $\lesssim 0.1\eta$ and 0.°05, respectively.

We regard the data discussed in this section as indicative rather than definitive for a number of reasons. Room-temperature measurements will not exactly reproduce the performance at 20 K. As discussed in the previous section, the 70 GHz bands may extend somewhat beyond the modelled frequency range of 60–80 GHz. At 30 GHz, OMT measurements were made only above 26.5 GHz, but in our model bandpass, 14–30% of the CMB power is received at lower frequencies; this is aggravated because the OMTs were designed for the nominal band of 27–33 GHz and so their performance below 26.5 GHz may be significantly worse than their measured in-band performance. Fortunately, the OMTs at this lowest frequency band have exceptionally high quality, and Table 3 shows that the out-of-band contamination would have to degrade the measured performance by an order of magnitude to cause a serious problem.

The main purpose of this section is to demonstrate the quality of the LFI OMTs. Even if the measurements were perfectly accurate, the values in Table 3 cannot be applied directly to the data since we have so far omitted the contribution of $\boldsymbol{J}^{\rm beam}$. Figure 6 shows that the cross-polar amplitudes fluctuate in sign across the band; therefore, we cannot simply combine the beam and OMT Mueller matrices; instead we have to evaluate the full Jones matrix chain at each frequency and then integrate across the band. This is expected to reduce the contribution of the OMTs to the depolarisation even further, for the following reason. We saw that conversion to V dominates the depolarisation, and Eq. (17) shows that this gives a net depolarisation irrespective of the sign of the cross-polar term. However, where $\boldsymbol{J}^{\rm beam}$ contributes significant V conversion, the OMT V term will (to first order) add to this, and is as likely to reduce the net V conversion as to add to it.

As a reality check on the electrical measurements, tests were performed using a pair of flight spare OMT/feed horn assemblies at 70 GHz. The measurements were made at IFP-CNR Milan, using the same VNA equipment used for the scattering matrix measurements (D'Arcangelo et al. 2009b; Villa et al. 2009; D'Arcangelo et al. 2009a). The two horns were mounted facing each other, and precisely aligned using a laser. A 70-GHz source was connected to one arm of one horn, and the detected power was measured in each arm of the other assembly as it was rotated around the horn axis. Position angles were measured to 0.°1 precision. The power-angle curves did not exactly match the expected sinusoidal pattern, partly due to drifts in the VNA power over the several hours required to complete the measurements. Significant sub-degree structure in the power-angle curves near the null points was likely due to reflections in the measurement set-up. Nevertheless the nulls for main and side arm were found to differ by 90° ± 0.°5, somewhat better than expected from the apparently systematic non-orthogonality reported from the flight model tests.

5.4. Beam Mueller matrices

The formalism discussed in Sect. 4.2 applies separately for every direction in the beam and frequency within the band. The components of $\mathcal{W}$ can be calculated from the Jones matrix elements using Eq. (12); for the beam component, the Jones matrix is

$$\boldsymbol{J}^{\rm beam} = \frac{1}{\sqrt{4\pi}} \begin{pmatrix} \text{Side co-polar} & \text{Side cross-polar} \\ \text{Main cross-polar} & \text{Main co-polar} \end{pmatrix} \tag{32}$$

where the terms in the matrix are the complex amplitudes calculated in our physical optics modelling of the beams. The factor of $1/\sqrt{4\pi}$ is derived in Appendix A. Using this we can calculate the angular distribution of each element of the top two rows of our Mueller matrix: in effect each element has its own beam. Figures 7–9 show these matrices of beams (excluding the V elements) for one LFI feed horn in each matched pair: the beams from each pair are close to mirror images of each other. These are derived from physical optics calculations identical to those described in detail by Sandri et al. (2010), except that, while those were based on the designed telescope and FPA geometry, the ones presented here are based on the radio frequency flight model (RFFM), which incorporates the measurements and thermal modelling of the flight-model hardware described by Tauber et al. (2010b). Departures from the design ideal have very little effect at 30 and 44 GHz, and even at 70 GHz cause no qualitative change to the patterns. These beams are computed at the nominal band-centre frequencies, and so do not take into account the slight variation of beamshape with frequency discussed in Appendix B.

As expected, the co-polar beam component strongly dominates, so that the diagonal components $\mathcal{M}_{II}$ and $\mathcal{M}_{QQ}$ are almost identical, as are $\mathcal{M}_{IQ}$ and $\mathcal{M}_{QI}$, both of which $\approx |J_{xx}|^2 - |J_{yy}|^2$. The cross-polar contribution changes sign between the members of these pairs, in principle causing differences, but they are much smaller than the (already small) difference between the co-polar beams which dominates both forward and reverse polconversion. In nearly all beams, the polconversion elements $\mathcal{M}_{IQ}$, $\mathcal{M}_{QI}$, and $\mathcal{M}_{IU}$ show a quadrupolar structure, indicating negligible beam squint between the main and side arms, but $\mathcal{M}_{QU}$, which governs angle errors, consistently shows a dipole structure.

The peak unwanted responses, relative to the copolar peak, are <1% for polconversion and <2% for $\mathcal{M}_{QU}$, except for the 44 GHz horns which are 2–3 times worse, especially LFI-25 and LFI-26 which are placed very far in the focal plane from the other LFI horns (Table 4). As discussed by Hu et al. (2003), since dipole and quadrupole patterns in the beam residual are on smaller scales than the nominal resolution, they alias high-ℓ modes to lower multipoles.

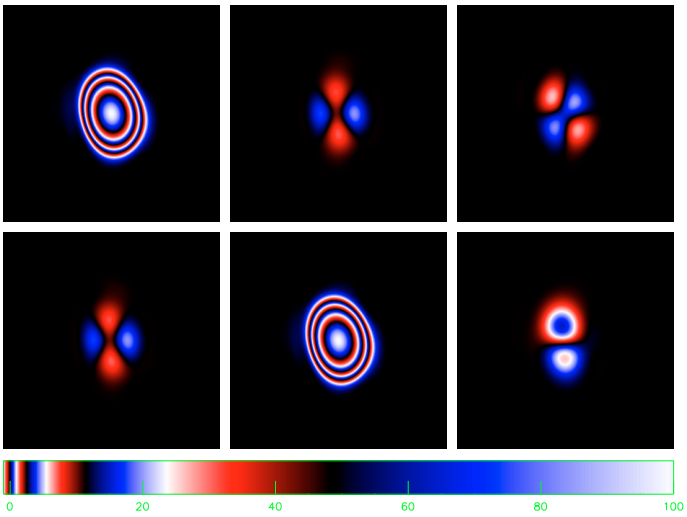

Fig. 7. Images of the beam Mueller matrix for LFI-27 at 30 GHz. *Top row* is $\mathcal{M}_{II}$, $\mathcal{M}_{IQ}$, $\mathcal{M}_{IU}$; second row is $\mathcal{M}_{QI}$, $\mathcal{M}_{QQ}$, $\mathcal{M}_{QU}$. The displayed region is 3.°78 on each side. For orientation, the co-polar polarisation direction is horizontal, and the centre of the focal plane is (roughly) on the right. Positive gain runs from black through blue to white, and negative from black through red to white. Saturated white corresponds to ±1% of the beam peak. The colour scale repeats (with non-linear scaling) for gains outside this range.

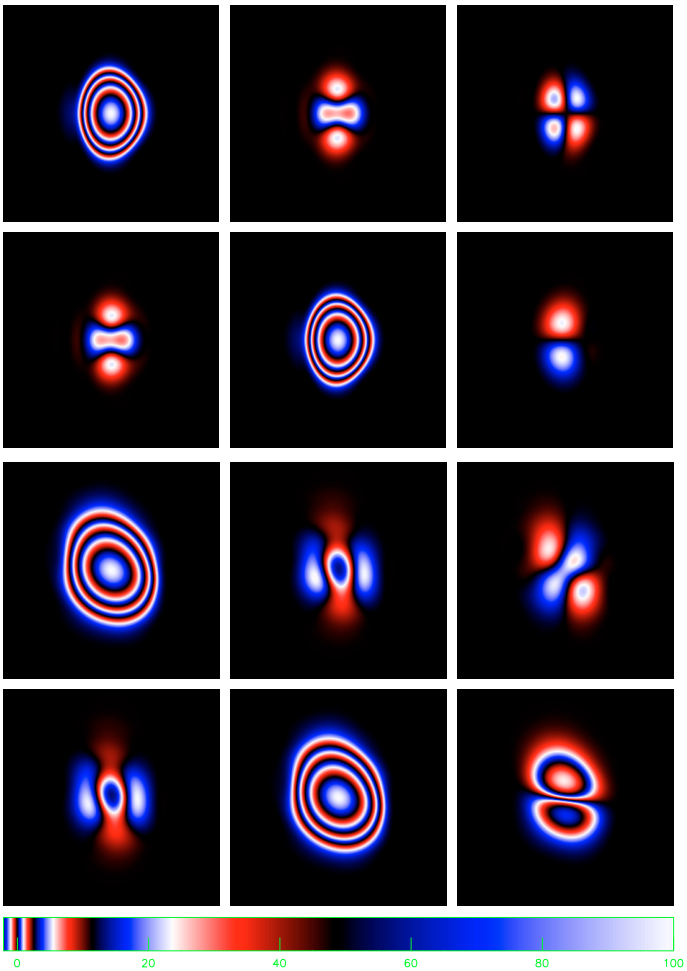

Fig. 8. Images of the beam Mueller matrix at 44 GHz: top: LFI-24, bottom: LFI-25. The displayed region is 2.°64 across; other details are as for Fig. 7.

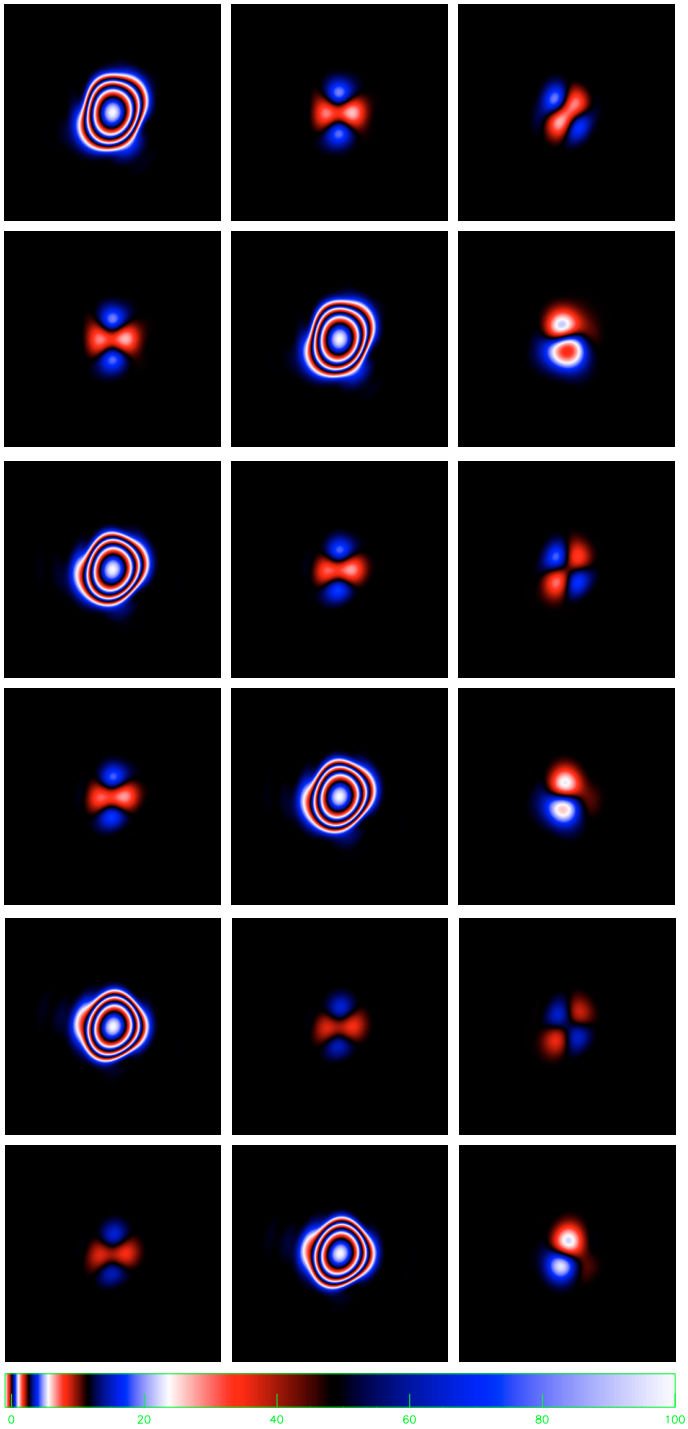

Fig. 9. Images of the beam Mueller matrix at 70 GHz for LFI-18 (*top*) LFI-19 (*middle*) and LFI-20 (*bottom*). The displayed region is 1.°72 across; other details are as for Fig. 7.

For large-scale structure ($1/\ell \gg FWHM$ beam), the effective polarisation response of the beam can be simply integrated over the beam area:

$$\langle \mathcal{M}_{IS}(\nu) \rangle = \int \mathcal{M}_{IS}(\hat{\boldsymbol{n}}, \nu)\, \mathrm{d}\Omega = \frac{1}{4\pi} \int (\mathcal{B}_{\mathrm{s}S} + \mathcal{B}_{\mathrm{m}S})\, \mathrm{d}\Omega \quad (33)$$

$$\langle \mathcal{M}_{QS}(\nu) \rangle = \int \mathcal{M}_{QS}(\hat{\boldsymbol{n}}, \nu)\, \mathrm{d}\Omega = \frac{1}{4\pi} \int (\mathcal{B}_{\mathrm{s}S} - \mathcal{B}_{\mathrm{m}S})\, \mathrm{d}\Omega, \quad (34)$$

where S stands for any Stokes parameter. From the normalisation of the single-detector beams, $\mathcal{B}_s$ and $\mathcal{B}_m$ (see Appendix A), forward polconversion $\langle \mathcal{M}_{QI} \rangle$ would be exactly zero if we integrated over the whole sphere. Table 4 lists the polconversions, cross-polar leakage η and rotations δ derived from these angle-integrated beams out to the maximum radius fully included in our main beam simulations, namely 1.°89, 1.°32, and 0.°86 at 30, 44 and 70 GHz. In all cases the unwanted components contains almost equal regions of positive and negative response within the main beam pattern, so that their integrated response is much smaller than their peak values.

Changes in the parameters listed in Table 4 between design and measured geometry are generally small: the largest fractional change in $\bar{\eta}$ was 16% (for LFI-24) and most changes were much smaller, so changes in Λ are all <0.1%. The largest change in $\langle \mathcal{M}_{QI} \rangle$ was <0.02%. Misalignments $\bar{\delta}$ changed by 0.°3 for LFI-25 and 26, and by $\lesssim$0.°2 for the other horns. Changes in the peak values of $\mathcal{M}_{QI}$ and $\mathcal{M}_{QU}$ were <0.5% except for LFI-25 and 26, whose peak $\mathcal{M}_{QI}$ actually improved over the design geometry by about 1%.

Errors associated with uncertainties in the geometry will be much smaller than these figures.

6. Susceptivity to focal plane temperature fluctuations

The susceptivity of the radiometer output to focal plane unit (FPU) temperature oscillations was evaluated using data acquired during the radiometer array assembly (RAA) cryogenic tests (Mennella et al. 2010). The LFI focal plane is cooled to approximately 20 K by a hydrogen sorption cooler (Tauber et al. 2010a; Morgante et al. 2009), and the sorption cooler cycling causes a small periodic oscillation in the temperature of the receiver front ends. During the RAA calibration campaign, a 100 mK peak-to-peak temperature oscillation was induced at the Sorption Cooler Interface as part of a "failure test". The FPU temperature is measured by sensors in various locations (for details see Bersanelli et al. 2010). We consider the sensor mounted on the LFI-28 feed horn, which is the closest to any radiometer. By analysing the correlation between the side−main output voltage difference of each RCA and the perturbing signal, we found a significant correlation for LFI-28 (Fig. 10). This is not the case for other radiometers, where the correlation is poor. From these data, it is possible to deduce the susceptibility function which links the temperature measured at each sensor to each RCA difference output.

The differencing was done using the raw output voltages (proportional to detected power), since it has not been possible to derive an accurate gain calibration, so the difference may partially reflect a gain mismatch. In any case, FPU temperature oscillations in operating conditions are much smaller (see Morgante et al. 2009), implying that this effect is likely to be negligible in flight. However the present analysis demonstrates that is possible to study this effect and to apply "non-blind" data cleaning methods.

7. Expected performance

7.1. The Planck scan strategy

The overall polarisation performance of the LFI is a global property of the survey, and so we briefly describe the strategy for scanning the sky (Tauber et al. 2010a). This is limited by thermal constraints requiring the spin axis to remain within 10° of the anti-solar direction during routine operations, with additional constraints on the angles to the Earth and Moon. As a result (cf. Fig. 1), possible scan paths are rather close to ecliptic meridians for latitudes $|\beta| \lesssim 40°$, i.e. more than half the sky. To allow scanning across the ecliptic poles the spin axis moves away from the Ecliptic in a cycloidal precession; the spin axis ecliptic coordinates (λ, β) as a function of the satellite anti-solar direction (λ_P, β_P) are given by:

$$\lambda = \theta \sin((-1)^n k\lambda_P + \Phi_0) + \lambda_p \quad (35)$$

$$\beta = -\theta \cos((-1)^n k\lambda_P + \Phi_0) + \beta_p, \quad (36)$$

where n gives the sense of cycloidal motion, k is the number of cycles per year, and Φ_0 is the reference phase for the pattern. The current baseline plan calls for reverse precession ($n = 1$), an amplitude of $\theta = 7.°5$, and $k = 2$ (six-month precession period). The simulations discussed below use these values except that in some cases $n = 0$, which inverts the patterns on the sky. The simulations ignore the ellipticity of the Earth's orbit and also the satellite's orbit around L2, and hence also ignore the variation in the angular speed of the spin axis motion.

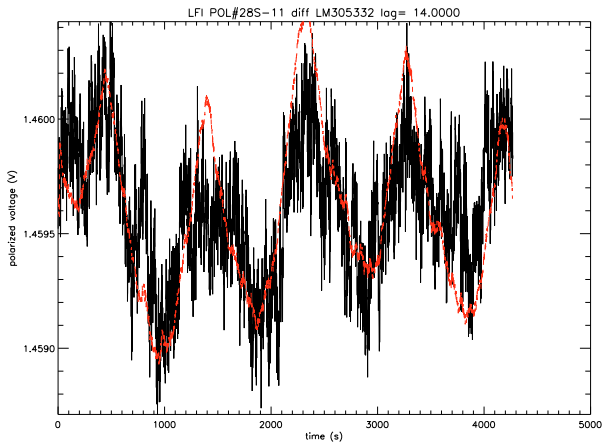

Fig. 10. Raw time-ordered side- minus main-arm differenced data (black) taken during cryogenic testing, plotted over temperature data (red, normalised, arbitrary units) for a sensor on the 30 GHz horn LFI-28. In order to show the correlation between the two time series, the temperature data were shifted forward by a time lag of 14 s, which had been evaluated by cross-correlating the raw and temperature data. This particular test is dominated by focal plane physical temperature oscillations induced by the sorption cooler (its 900 s period is clearly visible), since the thermal stabilisation system (TSA) was switched off to simulate TSA failure. These large (~100 mK) temperature fluctuations were convenient for establishing the temperature-dependent behaviour of each radiometer.

7.2. Sky coverage: polarisation isotropy

The scan angles χ of the two scans through most pixels differ from ±90° by less than 10° because of the near-meridian scanning, as already noted in Sect. 3.2 (cf. Figs. 1 and 12). With the unpaired horn at 44 GHz, and also minor deviations from the ideal symmetry of the focal plane in all bands, this small range of χ causes non-isotropic polarisation measurements, i.e. elliptical error distributions in the (Q, U) plane. We have simulated this effect for a typical *Planck* scanning strategy. Effects included were (i) slightly different scan patterns for the lead and trail horns, due to a tilt of 0.°2 of the spin axis from the satellite symmetry plane; (ii) rms $\bar{\delta} = 1°$ errors in the setting

Table 4. Key polarisation parameters of the LFI beams.

Feed	Band	Side arm		Main arm				Difference		
		$\eta_s{}^a$	$\delta_s{}^a$	$\eta_m{}^a$	$\delta_m{}^a$	$\bar{\eta}^a$	$\bar{\delta}^a$	$\langle \mathcal{M}_{QI} \rangle / \langle \mathcal{M}_{II} \rangle^b$	Max$(\mathcal{M}_{QI})^c$	Max$(\mathcal{M}_{QU})^c$
LFI-		10^{-3}	°	10^{-3}	°	10^{-3}	°	10^{-3}	%	%
18	70 GHz	1.91	0.23	2.03	0.23	1.97	0.23	−0.42	−0.82	1.75
19		1.33	0.09	1.46	0.09	1.40	0.09	−0.30	−0.75	1.19
20		1.06	−0.02	1.15	−0.02	1.11	−0.02	−0.15	−0.43	−1.11
21		1.05	0.02	1.11	0.02	1.08	0.02	−0.07	−0.31	1.14
22		1.33	−0.09	1.46	−0.09	1.39	−0.09	−0.29	−0.73	−1.22
23		1.91	−0.33	2.02	−0.33	1.96	−0.33	−0.34	−0.77	−2.04
24	44 GHz	1.84	0.00	1.70	0.00	1.77	0.00	0.27	1.43	1.05
25		4.58	−0.35	4.46	−0.35	4.52	−0.35	0.03	−2.14	−5.30
26		4.58	0.35	4.45	0.35	4.52	0.35	0.02	−2.16	5.32
27	30 GHz	2.19	−0.18	2.07	−0.18	2.13	−0.18	0.06	0.75	−1.87
28		2.19	0.18	2.07	0.18	2.13	0.18	0.05	0.76	1.86

Notes. All values are derived from beam models calculated assuming the adopted flight model telescope geometry (RFFM), evaluated at the nominal band-centre frequencies. $^{(a)}$ beam-averaged cross-polar leakage η and rotation δ; $^{(b)}$ beam-averaged forward polconversion as a fraction of the integrated gain; $^{(c)}$ absolute maximum values of the leakage for I and U_H into Q_H.

angles of each feed horn, (iii) rms 0.°5 errors in orthogonality between the two radiometer arms for each feed; (iv) rms 1% errors in polefficiency around a mean of 0.99;[8] (v) unequal weightings between horns due to their different noise levels, consistent with measured results (Meinhold et al. 2009); (vi) the unmatched LFI-24 and the slight departures from the ideal relative angle of 45° of the matched horn pairs noted in Table 1. As advocated in Sect. 3.1, we give equal weights to the two arms of each horn. From the discussion in Sect. 5, (i)–(iv) are worst-case assumptions; however, at 44 GHz, the polarisation asymmetry is completely dominated by the unmatched horn LFI-24, so the observed pattern is expected to be very close to this prediction.

The axial ratio of the (Q, U) error ellipse is plotted on the sky in Fig. 11. The mean axial ratio is 1.06, 1.38 and 1.07 at 30, 44, and 70 GHz. The 70 GHz pattern is not shown as it is very similar to that at 30 GHz. The patterns are essentially organised in ecliptic coordinates, but we show them projected in galactic coordinates to reveal more clearly the caustics around the ecliptic poles. These show up as regions of anisotropic errors because the coverage there is dominated by sets of locally tangential scans. Just outside these caustics are the regions where the scans cross at relatively large angles, significantly reducing anisotropy. At lower ecliptic latitudes, the axial ratio varies with longitude: it is reduced at pixels observed at cycloid phases near 0° (180°) for which the spin axis is maximally below (respectively above) the Ecliptic for the two scans through each pixel, maximising the relative angle between them; conversely, for pixels observed at cycloid phase near 90° or 270° the spin axis is on the Ecliptic and the two scans are parallel.

It is interesting to compare the sky coverage performance of *Planck* with WMAP, which relies entirely on the variation of χ between the scans through each pixel to break the degeneracy of using the same ψ for all horns, but which has a looser solar angle constraint. As might be expected, WMAP achieves worse polarisation anisotropy than *Planck*. Figure 11 shows the axial ratio distribution for the WMAP V band (patterns in the other bands are very similar). The detailed structure of the WMAP figure is largely due to the on-orbit events (safe modes, data edited for planet crossings etc.), which are not included in our *Planck* simulations. However, due to WMAP's observing mode of differencing beams separated by ∼1 rad, data editing has a much larger impact on WMAP than on *Planck*: in particular WMAP data in a beam at high latitude are flagged when its companion beam is pointing close to the Galactic plane, which inevitably introduces fine-scale structure into the coverage pattern.

The *Planck* simulations discussed here omit irregularities in the "hit count", i.e. the number of samples per pixel, caused by the discrete integration time and discretised scanning of the spin axis path. These effects cause random differences in the number of samples from the two matched horns on each scan circle that are assigned to a given pixel, and hence give pixel-scale fluctuations in the error anisotropy with rms 0.02.

7.3. Astronomical check on polarisation calibration

Due to the lack of ground calibration it is important to check the polarisation angle ψ of each horn using astronomical observations. Comparison with ground-based data is most accurate for a compact target source, and the only such object bright enough to give reasonable accuracy for the LFI is the Crab nebula (Messier 1, Taurus A, etc.), which has approximately 20 Jy of polarised flux density at LFI frequencies (Page et al. 2007). Since we would like to measure the misalignment $\bar{\delta}$ for each horn, we rely on the variation of scan direction between different scan paths. The ecliptic coordinates of the Crab (J2000) are $(\lambda, \beta) = (84.°097, -1.°290)$. Since it lies very close to the Ecliptic it is only visited twice each year, and the angle between scans depends critically on the phase of the cycloid scan pattern, as shown in Fig. 12. Given the limited amplitude of spin-axis motion around the Ecliptic, we cannot achieve the optimum scan-angle separation $\Delta\chi = 45°$, which would allow Q and U to be measured equally well. The actual $\Delta\chi \lesssim 15°$, which gives an error distribution in the (Q, U) plane with ellipticity ≳3.8. As Fig. 12 shows, the average of the two scan directions for pixels close to the Ecliptic is essentially along ecliptic meridians; hence, if the two detectors in the horn measure polarisation parallel and perpendicular to the scan direction ($\psi = 90°$ and 0°) then Q in ecliptic coordinates would be measured well and U badly; that is, the error ellipse would have its major axis along

[8] The error model is arranged to avoid $\Lambda > 1$.

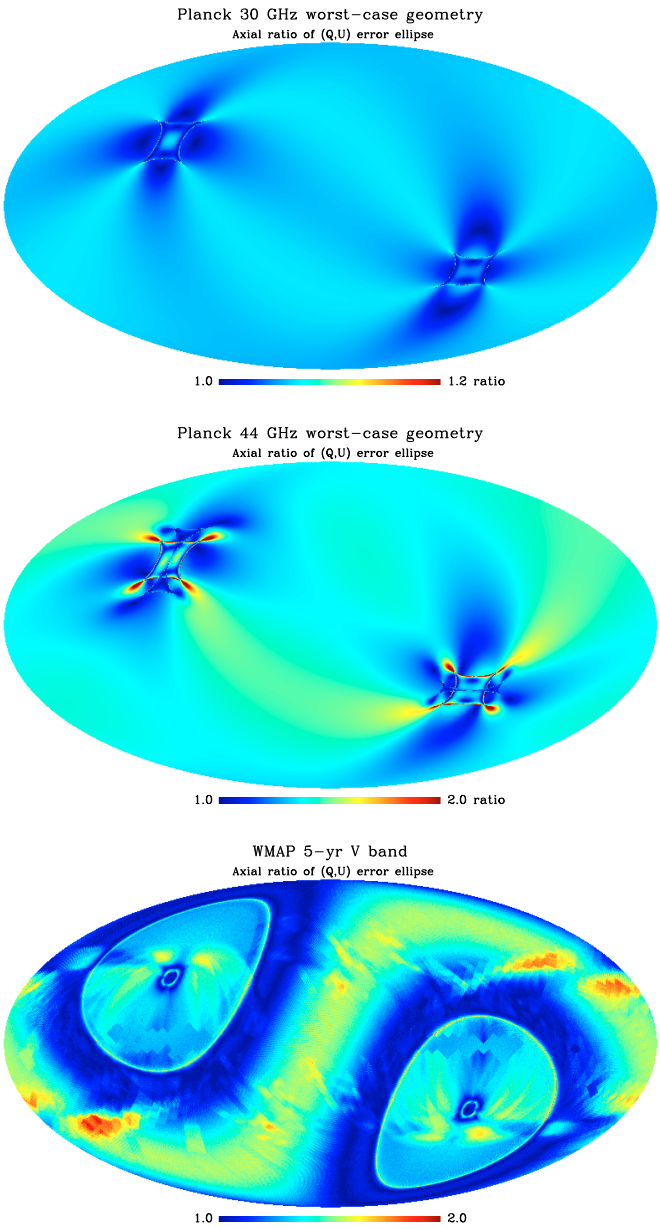

Fig. 11. Simulated pattern on the sky for the axial ratio of the (Q, U) error ellipse for worst-case geometric assumptions at 30 GHz (*top*) and 44 GHz (*middle*). Note that the colour scale for 30 GHz covers only 20% of the range for 44 GHz. Maps are in galactic coordinates. The actual pattern for the WMAP 5-year V band is show at bottom, on the same colour scale as for *Planck* at 44 GHz.

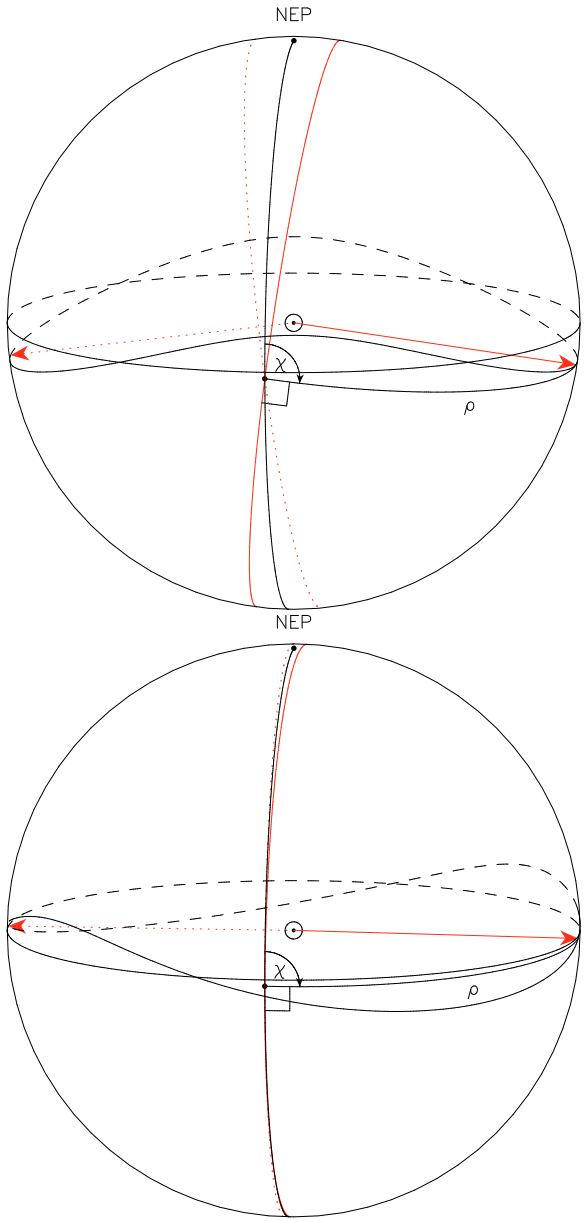

Fig. 12. Scanning the spin axis away from the Ecliptic allows us to obtain significantly misaligned scan circles even for a source like the Crab nebula that is sited on the Ecliptic. As in Fig. 1, red arrows and circles show the spin axis and scan circle, in this case for the two visits to the Crab in each year (the Crab is at the point just below the Ecliptic where the two scan circles intersect). The view is centred at ecliptic coordinates (90°, 10°). Also shown is the 180° period cycloid path of the spin axis (for $n = 0$). Top: near-optimal cycloid phase. Bottom: worst-case cycloid phase giving degenerate scans.

U (±90° in the (Q, U) plane). In general the error ellipse will be rotated from this orientation by 2ψ.

The Crab polarisation angle of ≈−88° in galactic coordinates (Page et al. 2007) translates to −28° in ecliptic coordinates, hence −56° in (Q, U). Therefore, for horns with $\psi = 22.^{\circ}5$, the major axis of the error ellipse is along 135°/−45°, within about 10° of the Crab's (Q, U) vector. As a result we get a relatively poor measurement of the polarisation amplitude but a good measurement of the angle. Conversely, for horns with $\psi = -22.^{\circ}5$ we get a relatively poor measurement of the angle.

Each LFI horn will make an independent measurement of the Crab from the two visits in each year of observations. Optimal fitting to the calibrated and background-subtracted time-ordered data will be used; that is, the known Mueller-matrix beam patterns for each detector ($\mathcal{M}_{QI}, \mathcal{M}_{QQ}, \mathcal{M}_{QU}$), synthesised over the band using the known spectral index of the Crab, will determine the weight of each sample of the $\tilde{Q}_{\rm H}$ signal, and the best-estimate (Q, U) will be derived by least squares fitting.

We have simulated the uncertainty in the Crab polarisation angle from this process, using the current best estimates for the LFI detector noise, and nominal background fluctuations with rms [17, 25, 25] μK at 30, 44, 70 GHz, respectively, for each of Q and U. The fluctuation values are upper limits to the signal (as opposed to noise) fluctuations derived in annuli around the Crab in the WMAP 5-year maps, for the nearest frequency channels.

Results are shown in Fig. 13. The primary variable is the reference phase of the cycloid scanning strategy, Φ_0. The approximate orbit used in our simulations[9] does not affect the basic geometry, in particular the phases at which the scan angles become degenerate and hence the errors diverge, at $\Phi_0 \approx 65°$ and 275°. For $n = 0$ (forward precession) the major change is that the scan degeneracies occur at $\Phi_0 \approx 115°$ and 265°. Avoiding these bad phases is one of the more significant constraints on the choice of scan strategy.

The figures show that we can obtain precisions of better than 0.°5 degrees for about half of the RCAs, with only the three awkwardly-oriented RCAs at 70 GHz being significantly worse than 1°. Where the uncertainty is approximately constant with Φ_0, the errors are dominated by our assumed background fluctuations; these are 1σ upper limits and may be significant overestimates at 44 and 70 GHz, since they are derived from WMAP Stokes Q and U data at Q, V, and W bands where there is no secure detection of fluctuations in our background annuli.

These measurements determine the relative orientation of the feed horn to the Crab's net polarisation angle Θ at the effective observing frequency. This will unambiguously reveal any misalignments between feeds in each band, but to give us the desired absolute angle we need external measurements of $\Theta(\nu)$. Theory tells us that the polarisation of a synchrotron source such as the Crab will change only very slowly with frequency in the Faraday-thin regime. Faraday rotation in the Crab has a mean rotation measure $RM \approx -23\,\mathrm{rad\,m^{-2}}$ and an rms of $\sigma_{RM} = 14\,\mathrm{rad\,m^{-2}}$ (Bietenholz & Kronberg 1991); this corresponds to rotations of 0.°08 at 30 GHz, which we can indeed neglect. The remaining effect is that the Crab's net polarisation is a vector average over the rather tangled polarisation structure of the nebula; since the spectral index is not exactly the same at all positions in the nebula, the weighting in the average changes slowly with frequency. Fortunately, over the LFI band such spectral index variations are remarkably small: Green et al. (2004) show that the spectral index between 1.5 and 350 GHz varies by ≈±0.02 over the bright part of the nebula, which dominates the total flux, corresponding to a change of weight of typically ≈±1.7% between 30 and 70 GHz.

The current best direct measurements of the Crab polarisation in the LFI frequency range are those from WMAP. Page et al. (2007) presented preliminary measurements based on simple aperture photometry, with typical errors of 1°–3°, but we estimate that with optimal fitting, the 5-year data will yield random errors (including background fluctuations) ranging from 0.°14 at K band to 0.°9 at W band. Page et al. estimate that their absolute orientations are known from pre-launch data to <0.°5; this systematic uncertainty will dominate except at W band. Indeed, we have made a fairly simplistic analysis of the released 5-year data which demonstrates consistency of the Crab polarisation angle between channels at this level. We intend to supplement the WMAP results with new ground-based measurements, but this will require *ab initio* determination of the instrumental polarisation angles, since up to now there has been no scientific motive to calibrate absolute angles of conventional radio telescopes to better than ≈±1°[10].

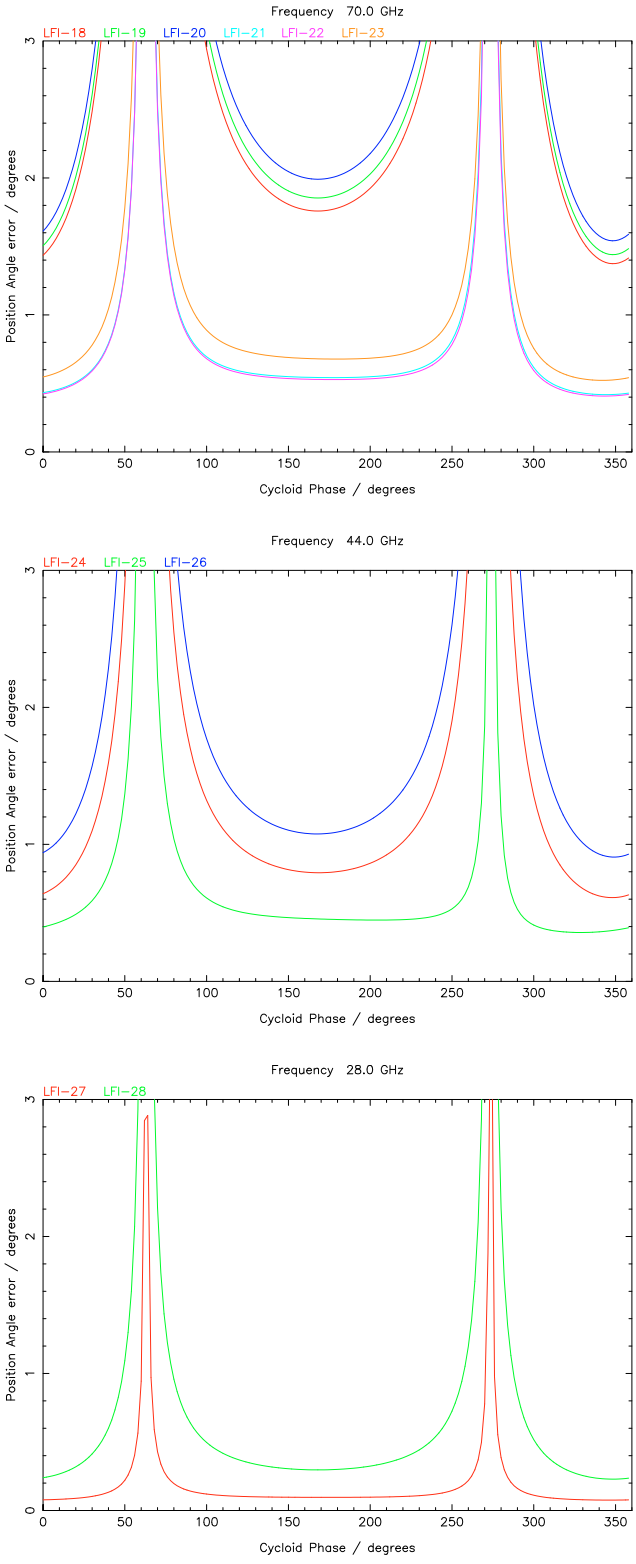

Fig. 13. Estimated error in single-horn position angle measurement of the Crab nebula as a function of cycloid phase Φ_0 (see text), assuming reverse precession ($n = 1$).

These observations of the Crab nebula will allow a careful check of our nominal position angles for a subset of RCAs. As discussed in Sect. 3.2, there is some reason to believe that the true angles should be very close to nominal, so only highly significant discrepancies would justify actual revision of the angles

[9] The major shortcoming is that our simple model omits the variation in sensitivity caused by the slightly different rate of scanning over the Crab on different visits.

[10] The usual procedure is to refer all angles to a nominal value of 33° for 3C 286 (e.g. Perley 1982). This value has been in use since the mid 1970s, apparently based on an analysis of earlier absolutely-calibrated data, but no details or uncertainty have been reported.

stored in the LFI instrument model, which are used for calibration and map-making. However, less significant discrepancies might justify increasing the nominal uncertainties. While the Crab is the only suitable target for linking the polarisation angle calibration to ground-based measurements, observations of bright diffuse polarisation in the Galactic plane may allow relative calibration between horns within each LFI band; in particular this may allow us to transfer accurate position angles at 70 GHz to the three horns for which Crab calibration does not work well.

7.4. Zero levels and destriping

Fundamentally differential experiments like *Planck* and WMAP are incapable of determining the absolute zero level in total intensity. This missing monopole (and also the relatively ill-determined dipole) is unimportant for CMB anisotropy analysis but is a significant issue in modelling foreground emission (Eriksen et al. 2008). The equivalent issue for polarisation is quite subtle. At first sight there is no problem, since the spin-2 harmonic expansion used for polarisation contains no monopole or dipole terms. However, this does not prevent Q and U maps from containing spurious monopoles and dipoles: harmonic analysis converts these into higher-ℓ components in E and B. Furthermore, $1/f$ noise ensures that the $\tilde{Q}_{\rm H}$ signal will indeed contain a large, slowly-varying offset. *Planck* observes by spinning around an effectively fixed axis, completing 30–50 revolutions at each spin axis position. Averaging the data onto the scan circle therefore strongly suppresses noise except at harmonics of the spin frequency. The LFI receivers are designed so that the $1/f$ noise is below the white noise for frequencies less than about 2–3 times the spin frequency; hence the major impact of $1/f$ noise is a large spurious offset on each scan circle; in addition there is a spurious dipole of the same order as that due to white noise. When binned into a map, the offsets contribute to all multipoles. Due to symmetries of the scanning strategy, the resulting map dipole is an order of magnitude below the monopole.

However, unlike the case of total intensity, the spurious offset in $\tilde{Q}_{\rm H}$ does not render the true zero-level of the sky images unmeasurable, because of the variation of the orientation of $Q_{\rm H}$ with respect to the sky coordinates along the scan circle. As a simple example, consider the case where $\rho = 90°$ and the spin axis has $\beta = 0$, so that scanning is along ecliptic meridians (Fig. 14). Suppose that the offsets measured along the scan at longitudes 0°, 180° (red line) correspond to a spurious polarisation at the north ecliptic pole as shown by the black double-headed arrow. This spurious polarisation is parallel-transported along the scan path, hence giving rise to the red double-headed arrow at the south ecliptic pole. Now consider the scan at longitudes −45°, 135° (green line). If its offsets give the same spurious polarisation at the NEP, after parallel transport to the SEP the orientation is given by the green double-headed arrow, which is rotated by 90° relative to the offset on the red line; that is the signs of Q and U are reversed.

Evidently, in this simple case, the offsets can be determined by taking the difference of the measured (Q, U) along the two scans at the two poles, which gives respectively the sum (south pole) and difference (north pole) of the offsets on the two scan lines. This particular arrangement is far from optimal: only of order one beamwidth of data are used to determine the offset on each scan circle; furthermore spurious modes consisting of a mixture of monopole and dipole of the form

$$\mathcal{S}(\lambda,\beta) = \mathcal{S}_0\,(\cos 2\lambda + \sin\beta \sin 2\lambda) \qquad (37)$$

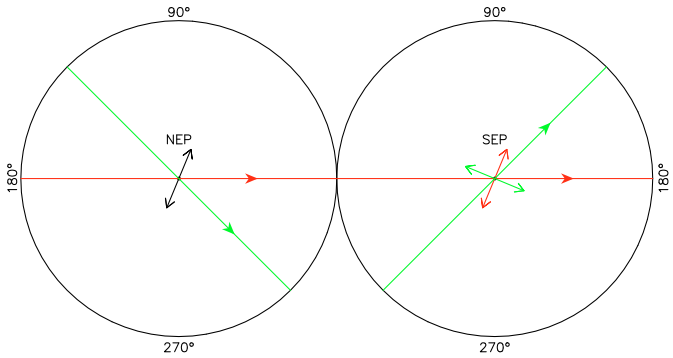

Fig. 14. Illustration of the interaction between offsets on different scan circles. Scan circles along ecliptic meridians separated by 45° transport the same polarisation at the north ecliptic pole (NEP), shown as the black double-headed arrow, to orthogonal polarisations at the south pole(SEP).

cannot be distinguished from real polarisation structure. For *Planck*'s actual scan strategy, scan circle crossings at substantial angles occur over about ±20° around the poles, so that a much longer run of the circle is involved in constraining the offsets, giving higher signal to noise, and also reducing the sensitivity to monopole-dipole degeneracy.

The actual determination of the offsets will be made in the course of iterative destriping, for instance using the MADAM algorithm (Keihänen et al. 2005; Keihänen et al. 2010; Ashdown et al. 2007; Kurki-Suonio et al. 2009).

Based on running MADAM on simulated 70 GHz data, we estimate that the residual Q and U monopoles and dipoles due to $1/f$ noise are at most about 3 (for $f_{\rm knee} = 50$ mHz) or 2 (for $f_{\rm knee} = 25$ mHz) times as large as expected from random white noise. The 44 GHz and 30 GHz detectors have a lower sampling rate, giving worse statistics to determine the offsets. Therefore the residual monopoles and dipoles may be about 25% (44 GHz) and 50% (30 GHz) higher relative to white noise than for 70 GHz.

7.5. Gain calibration

7.5.1. Overview

The primary gain calibration of the LFI against the CMB dipole is discussed by Cappellini et al. (2003). For a scan circle radius ρ, and an angle ζ between the spin axis and the dipole vector, the scan samples angles in the range $\rho \pm \zeta$ from the dipole peak, and hence the amplitude of the dipole signal on the scan circle is $D = D_0 \sin\rho \sin\zeta$, where $D_0 = 3.358 \pm 0.017$ mK (Hinshaw et al. 2009) is the full-sky dipole amplitude. For present purposes, we can take $\rho \approx 90°$, so $D \approx D_0 \sin\zeta$. This fluctuates substantially over the survey, since the cosmological dipole vector is close to the Ecliptic ($\lambda, \beta = 171.°65, -11.°14$), so that in March and September $\sin\zeta$ becomes small. Due to the 6-month precession of the spin axis, one pole is approached closer than 11.°1, and the other pole somewhat further away; for an amplitude of 7.°5 the possible range is 3.°6–18.°6 and if the phase choice is based on optimising the Crab scan angles, as currently expected, the actual approach angles will be close to the minimum and maximum values[11]. The corresponding net amplitude

[11] The ≈300 μK dipole due to the satellite's orbital motion around the Sun does not affect this range as it merely shifts the net dipole along the Ecliptic without affecting the out-of-plane component which contributes the residual dipole signal at closest approach.

minima are $D = 0.21$ and 1.07 mK, compared to a median value of $D \approx D_0 \sin 45° = 2.4$ mK. Thus, although typically the dipole allows calibration to $\lesssim$1% in an hour (Sect. 5.1), during the lowest dipole period the calibration precision will be ten times worse than the median.

In addition to the CMB dipole, a strong signal is available at each crossing of the Galactic plane. Unfortunately this has a different spectral shape from the CMB and therefore a different "colour correction" (see Sect. 5.2). Further, we do not have accurate prior knowledge of the Galactic brightness at LFI frequencies. Therefore the brightest parts of the Galactic plane will be masked and the remainder modelled and subtracted when deriving gain factors. Similarly, as noted by Cappellini et al., the CMB fluctuations themselves can be a significant source of error, especially during low-dipole periods, if no correction for them is made. Fortunately, calibration errors are a second-order effect, so the CMB fluctuations and high-latitude foregrounds can be mapped with sufficient accuracy to correct for their effect on calibration even before final gain values have been derived.

7.5.2. Analysis of simulations

To assess the impact of random errors in the gain calibration on the polarisation maps, we re-analysed the "Trieste" simulations made by Ashdown et al. (2009). These were simulated observations by the *Planck* 30-GHz system, with a fairly realistic scan strategy in a 1-year survey. In the simulation, the spin axis was fixed for 1-h "pointing periods" (actual pointing periods will be shorter on average and have variable lengths). At the two periods of dipole minima, the dipole amplitudes were 0.49 and 0.81 mK, so this is not as asymmetric as the likely flight pattern. The annual dipole was not included but would have made very little difference for the assumed scan strategy. The model sky comprised many components, including polarised Galactic foregrounds, but realism was not a high priority; in particular, the Galactic plane is much too highly polarised in the light of WMAP results.

Simulated timelines for foregrounds, CMB, dipole, and noise were prepared separately, facilitating our analysis. We re-scaled the noise to values consistent with those reported by Meinhold et al. (2009), and the calibration procedure was simulated by fitting the dipole+destriped noise to find a gain factor for each pointing period. We refer to this as case B (case A will follow). This does not include the iterative procedure needed to correct for CMB fluctuations and foregrounds. Our error estimates are optimistic, since they do not account for masking of the strong foreground features, in particular the Galactic plane; in general this will affect only a small fraction of each scan circle but it happens to have its largest impact when the dipole signal is weakest, as we see below. Figure 15 shows an example run of estimated gain differences: the increased scatter in March and September is obvious.

We also simulated the impact of ignoring the CMB fluctuations by fitting the CMB + dipole + noise to a dipole (case A). As expected the residual errors were much larger ($\sigma_\gamma = 1.2\%$ vs. 0.3% per hour over the full year), but also as expected, they are highly correlated between the main and side arms, since the CMB fluctuations are predominantly unpolarised; in fact plots such as Fig. 15 for the two cases are virtually indistinguishable. This is the term that controls polconversion (Eq. (9)), and evidently it is highly insensitive to errors in modelling the non-dipole emission.

The data for each polarisation of each detector were multiplied by the appropriate gain factor to simulate random calibration errors, and the $\tilde{I}$ and $\tilde{Q}_H$ signal streams were used to create maps of (I, Q, U), using the MADAM destriping mapmaker (Keihänen et al. 2005; Keihänen et al. 2010), as in the original analysis by Ashdown et al. (2009). We also produced and mapped a second set of timelines where the calibration factors had been averaged for 6 days by simple binning. Since MADAM is a linear process it is meaningful to analyse signal-only maps to isolate the errors due to miscalibration. Figure 16 shows the difference between the signal-only maps with and without the residual gain errors, for Stokes I and Q.

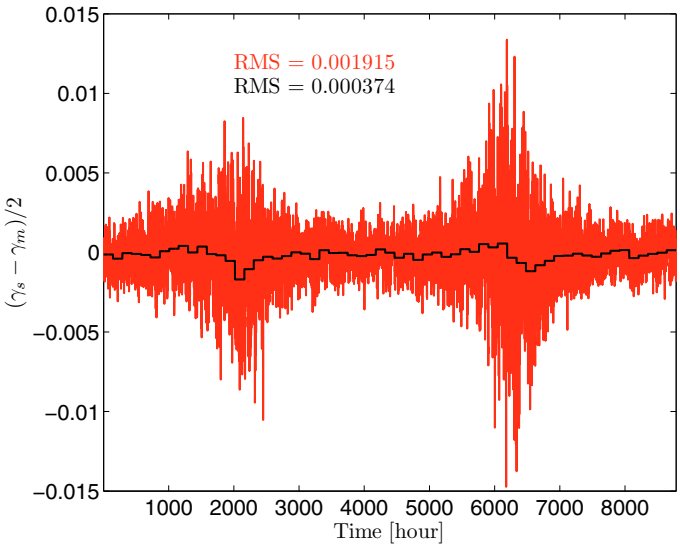

Fig. 15. Gain error difference $(\gamma_s - \gamma_m)/2$ between side and main arm radiometers of the LFI-27 horn. The plot is for a 1 year survey. Red line: gains were obtained by fitting the dipole signal to each 1-h pointing period. Black line: 6-day binning of the 1-h gains. The RMS values give the standard deviation of 1-h and 6-day gain error differences.

As expected for a multiplicative effect, the largest residuals are along the Galactic plane. At high Galactic latitudes the systematic variation of gain precision is not apparent, because the residuals are proportional to γI, where I is the local sky signal and is dominated by the dipole. Since γ, the fractional calibration error, is inversely proportional to the dipole signal on the scan circle, the rms value of γI does not vary systematically with ecliptic longitude; instead a strong ecliptic latitude effect is seen due to the increasing density of scan crossings in the deep regions near the poles, mirroring the pattern for white noise. At low Galactic latitude the situation is different because the strong Galactic signal is not used for the calibration. The relatively large gain errors during the two low-dipole periods give rise to large residuals along the corresponding scan circles, near ecliptic longitudes 90° from the dipole direction, which cross the plane at Galactic longitudes of 170° and 350°, and also cross the bright Orion complex near the anticentre. These scans cross the plane at a relatively small angle, so masking the plane will affect a significant fraction of the scan length, further degrading the calibration; this awkward geometry is fixed by the relative orientation of the dipole and the Galaxy.

The amplitudes of the residuals for I and Q are rather similar, since the Q residuals are mainly due to polconversion from I and not to distortion of the true Q signal. The magnitude of the on-sky residuals is significantly smaller than the naive estimate of $|\gamma I|$, because each pixel contains contributions from several independent pointing periods and detectors.

While ideally we would have run a Monte-Carlo series to characterise these errors, a single realisation gives a

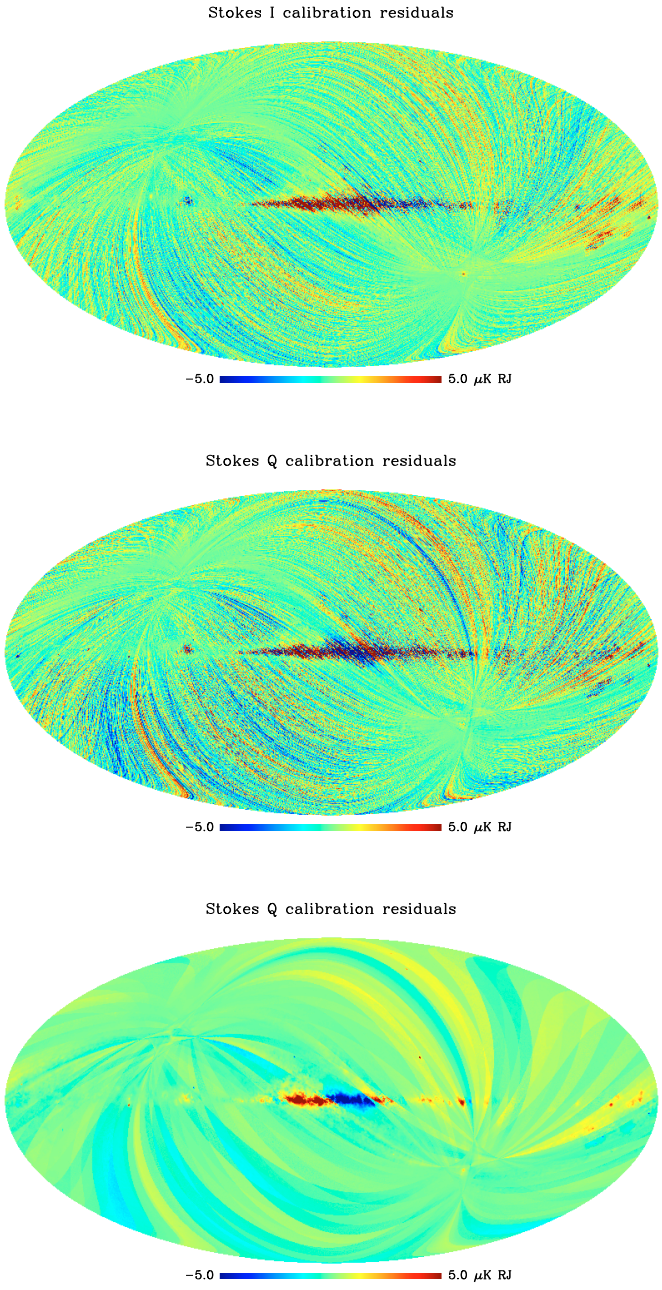

Fig. 16. Residual errors due to gain miscalibration in a simulated 1-year survey at 30 GHz. *Top*: Stokes I with 1-h solution periods for the gains; *Middle*: Stokes Q; *Bottom*: Stokes Q using 6-day averaged gains. Stokes U shows a similar pattern.

reasonable estimate, given the 3 million pixels in our map (HEALPix $N_{\rm side} = 512$). Table 5 characterises the errors at the pixel level by comparing the residuals (as displayed in Fig. 16) to the expected white-noise rms in each pixel. Even for 1 h averaging, the ratio is almost always much less than unity, rms 3%, with just a few pixels on the Galactic plane being slightly dominated by gain errors. Errors at these points are a few tenths of a percent of Stokes I. Going to 6 days (144 h) averaging does not reduce the rms by $\sqrt{144} = 12$, but only by a factor of 2–3, since substantial averaging is already obtained by binning into the sky pixels, as noted above. These numerical results depend on the chosen pixel size: both the calibration residuals and the white noise would be smaller for larger pixels; however while

Table 5. Statistics of the ratio of the calibration error residuals (i.e. difference between noiseless maps with and without calibration errors) to the expected white noise variance in each pixel.

Averaging time	Stokes	rms	Min	Max
1 h	I	0.033	−1.72	2.05
1 h	Q	0.030	−1.34	1.25
1 h	U	0.030	−1.55	1.20
6 days	I	0.016	−0.26	0.64
6 days	Q	0.011	−0.17	0.36
6 days	U	0.011	−0.47	0.40

the white noise variance is inversely proportional to the number of samples per pixel, which is proportional to pixel area, for calibration errors, numerical experiments show that the variance scales roughly as $D^{-1/2}$ for 1-h averaging. (For 6-day averaging the calibration errors are already correlated on larger scales than individual pixels as shown by Fig. 16, so pixel size has negligible effect.) Hence the typical rms values for 1-h calibration in Table 5 should scale by $(D_{\rm pix}/6.87\,{\rm arcmin})^{3/4} = (512/N_{\rm side})^{3/4}$. Since we expect to use $N_{\rm side}$ in the range 256–1024 for LFI maps, this variation will not alter the conclusion that gain errors are generally negligible at the pixel level.

The same arguments suggest that gain errors will have their largest effects in the C_ℓ at low multipoles. The simple scaling in the previous paragraph breaks down when averaging over large regions, because the calibration residuals decorrelate due to structure in the Stokes I map as well as due to variation of the gain errors. Figure 17 shows angular power spectra for temperature and E-mode polarisation of the gain residuals, for both 1-h and 144-h solutions. Averaging only has an effect on the residual spectrum at high ℓ, because the low-ℓ residuals are driven by the component of noise fluctuations which are correlated over large separations on the sky, and hence over long periods in the time line. Hence averaging the solutions has negligible effect at $\ell \lesssim 20$ for case B (and at $\ell \lesssim 100$ for case A, where the "large-scale correlated noise" is the CMB structure, dominated by the first acoustic peak).

On the very largest scales ($\ell \lesssim 10$) the rms calibration residuals slightly exceed the white noise in temperature, and are very close to this level in E and B. This remains true (but less so) for a WMAP-like Galactic cut. In practice, on these scales the white noise is smaller than the $1/f$ residuals which in turn are likely to be smaller than residuals from separation of the CMB from foreground components. Further, cosmological interpretation of the temperature (but not polarisation) angular power spectrum at low ℓ is limited by cosmic variance, which is much larger than both foreground and gain residuals.

Although we have only analysed simulations at one frequency band, the ratio of gain residual to noise is expected to be essentially the same at all LFI bands. Gain residuals are $\propto \gamma I$, while the rms γ is $\propto \sigma_T/D$ for one detector (Eq. (23)). Thus, in the sky maps both gain residuals and white noise scale as $\sigma_T/\sqrt{N_{\rm det}}$, and their ratio fundamentally depends on the ratio of local sky signal to calibration signal, I/D, which is frequency independent in LFI bands because both are dominated by the CMB dipole. Sect. 5.1 suggests that gain drifts may begin to be significant on periods of 1 h. Figure 17 shows that if we calibrate on this timescale we can reduce the rms calibration errors to well below the white noise level for $\ell > 20$. Signals below the white noise level are still detectable by binning C_ℓ, and Fig. 17 shows that in the polarisation spectra, 1-h residuals are close to the C_ℓ uncertainties for coarse binning ($\Delta\ell = 0.3\ell$), so we may need

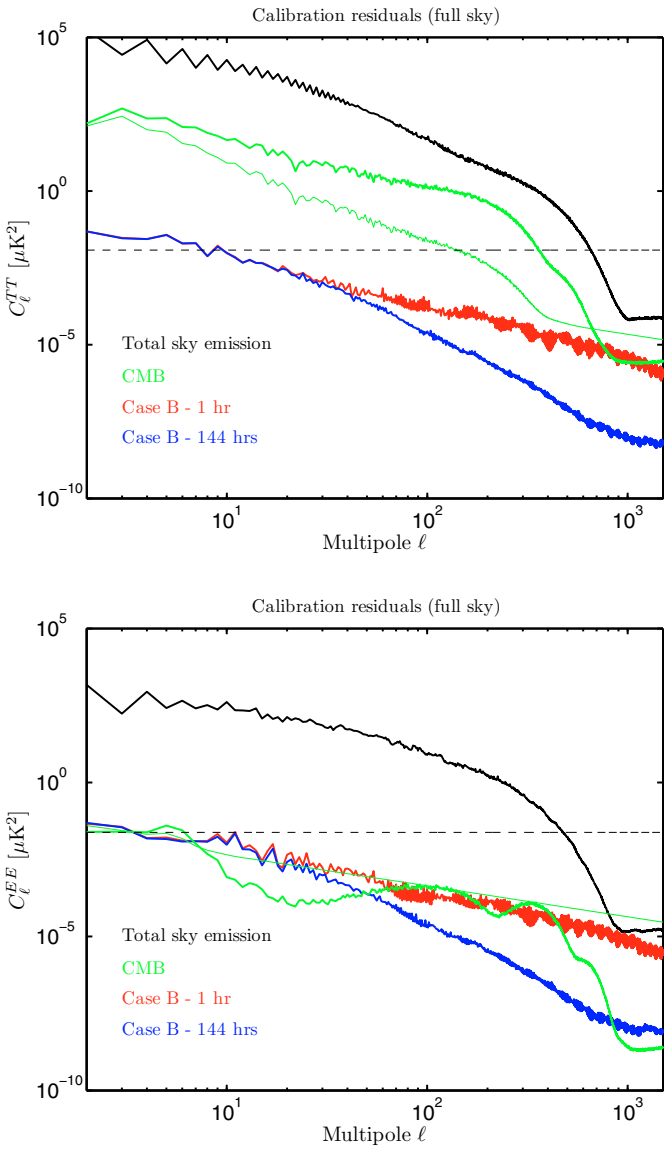

Fig. 17. 30 GHz angular power spectra of the calibration residuals compared with the power spectra of the CMB and total sky emission including foregrounds. *Top*: temperature; *Bottom*: *E*-mode polarisation. The thick green line shows the (noiseless) CMB spectrum. The thin green line is its error (standard deviation) for uniform map weighting, 30% ℓ bins ($\Delta\ell = 0.3\ell$) and 12 months observations. The horizontal dashed line is the white noise spectrum of the map expected in flight (Meinhold et al. 2009). The C_ℓ error includes cosmic variance and noise. No Galactic cut has been applied: such a cut brings the full-sky spectrum closer to the CMB-only spectrum but has only a modest effect on the calibration residuals. The *B*-mode polarisation spectrum is similar to *E*-mode, as might be expected since both are dominated by polconversion from *I*. The flattening at $\ell \gtrsim 1000$ is due to pixel aliasing, see Ashdown et al. (2009). (Note: WMAP data show that the foreground polarisation in these simulations is too bright by nearly an order of magnitude, or nearly 10^2 in C_ℓ).

to subtract an estimate of the calibration residual power spectrum to avoid being dominated by this systematic. These will be generated from monte-carlo analyses, which will automatically take into account the expected correlation between gain error residuals and the white noise. This analysis also shows that gain errors are only important at map pixel level for the strongest polarisation signals, namely compact Galactic peaks and the lowest-ℓ diffuse structure. Of course, gain errors can be quantified and included in the pixel error model.

7.6. Impact of non-ideal beams

CMB map-making conventionally assumes a delta-function beam, and corrects for finite-beam effects in the angular power spectrum (C_ℓ) using a window function (e.g. Bond et al. 1998; Netterfield et al. 2002). Rosset et al. (2007) analysed the impact of non-ideal beams on CMB polarisation using a flat-sky approximation observed with simulated *Planck* HFI beams at 143 GHz (which are relatively circular); Ashdown et al. (2009) studied the same effects on all-sky data including foregrounds, using models of the much more elliptical 30 GHz beams, based on the physical optics simulations described by Sandri et al. (2010). However, Ashdown et al. included only the co-polar patterns. As discussed above, polconversion is driven by the co-polar beams and so this effect was well represented, but the $\mathcal{M}_{QU}$ term depends on the cross-polar pattern (Eq. (12)) and so was omitted. Because this component rotates the apparent polarisation direction on the sky it converts *E*-mode to *B*-mode polarisation. *E*-to-*B* leakage is also caused simply by having non-identical beams for *Q* and *U* measurements, even if each beam is perfectly co-polar. As Fig. 2 shows, *Q* and *U* beams for the LFI differ significantly in orientation, and Ashdown et al. confirmed that this caused substantial distortions in the recovered polarisation spectra in noiseless simulations. As expected from the analysis of Hu et al. (2003), the distortions are at multipoles corresponding to the beam scale, $\ell > 1/FWHM$, and are especially severe for the extremely faint *B*-mode spectrum. However, for the LFI these C_ℓ are below the white noise level, except for distortions of the *T*–*E* correlation spectrum. Polarisation distortions due to non-ideal beams also have a substantial impact around bright polarised sources in the image, such as Galactic nebulae.

Several procedures have been proposed for correcting these distortions. Rosset et al. (2007) find that, for their relatively symmetric beams, the temperature and *E*-mode polarisation maps are recovered with little distortion. They therefore use these to predict and correct for the leakage of *T* and *E* into the *B*-mode polarisation.

Ashdown et al. (2009) describe an extension of window-function methods, which predicts and corrects the leakage between temperature, *E*-mode, and *B*-mode in C_ℓ. This methods relies on the statistical isotropy of the polarisation pattern, while the Rosset et al. approach relies on the polarisation being dominated by *E*-modes; therefore neither are likely to perform well when applied to data strongly contaminated by Galactic foreground polarisation. In fact WMAP shows that the polarised synchrotron component that dominates at LFI frequencies is significantly weaker than the CMB *E*-mode on the beam scale, after masking out the Galactic plane and other strong features covering ~25% of the sky; so these methods are expected to yield useful results. Nevertheless, one of *Planck*'s advantages compared to WMAP is its superior frequency coverage, which is designed to allow much more accurate foreground modelling and subtraction and hence the exploitation of a larger fraction of the sky for CMB analysis. Therefore, more effective procedures are desirable to allow correction of beam asymmetries in regions strongly affected by foregrounds; of course this is also needed for astrophysical analysis of foregrounds. Some promise is shown by deconvolution techniques such as PReBeaM (Armitage-Caplan & Wandelt 2009) which aim to recover the sky convolved with a suitable "regularising" beam, i.e. a symmetric beam

comparable in size to the original asymmetric beam. The FICSBell code of Hivon and Ponthieu, mentioned by Ashdown et al. (2009), obtains a similar effect via map post-processing rather than incorporation of deconvolution in the map-making. A fail-safe approach is reconvolution, in which the data are interpolated onto the sky grid to yield the sky convolved with the smallest symmetric beam that contains the actual one. Such techniques may be useful for constructing accurate foreground models based on low- and high-frequency channels, which can be applied as small corrections to conventional maps in the central CMB-dominated bands. We do not expect to use deconvolved maps for extraction of CMB power spectra, since error propagation becomes computationally unfeasible: for analytic propagation, they correlate the noise between nearby pixels, vastly increasing the size of the matrices that need to be inverted; for Monte Carlo analysis (used to account for residual $1/f$ noise in the map), deconvolution increases the data-to-map processing time by about two orders of magnitude. (Reconvolution is fast, but sacrifices signal at high ℓ).

8. Conclusions

We have described the main instrumental parameters that affect the polarisation response of the *Planck* LFI, as far as they are known at the time of launch. The LFI has the potential to measure the CMB E-mode polarisation power spectrum more accurately than any experiment to date, and will also make high signal-to-noise measurements of the polarisation of the low frequency foreground emission, which is essential for correcting foregrounds in the *Planck* maps and very likely will also be used to correct maps from future dedicated CMB polarimetry experiments.

In most respects the LFI is an excellent polarimeter with very low systematics. Depolarisation by the optics and by imperfections in the OMTs which separate the orthogonal linear polarisations is almost negligible, and is accurately measured so that it can be corrected with effectively perfect accuracy. Stokes parameters Q and U will be measured with almost equal accuracy at all pixels at 30 and 70 GHz, and with only mild anisotropy at 44 GHz. Relative gain calibration using the CMB dipole is accurate enough that this will be a negligible source of conversion from total to polarised intensity, especially if gains drifts at the 1% level have timescales of months as we suspect; in-flight measurements will quantify such fluctuations and allow us to optimise our gain calibration strategy accordingly.

Some important instrumental parameters have not been definitively measured during the pre-launch campaign and will require on-orbit calibration together with further analysis of the Flight Spare hardware. For example our estimate of the 30 GHz OMT performance between 23 and 27 GHz will be refined based on measurements of the flight spare, and the current bandpass modelling procedure will be checked against improved measurements of the flight spares.

A notable uncertainty is the effective polarisation angles of the feed horns: while these are certainly known to the 3° accuracy required for direct observations of the CMB, in-flight calibration is required to confirm our aspired 0.°5 degree accuracy, which would make the LFI maps a fundamental resource for foreground correction of future experiments targeting B-mode polarisation. We have shown that most LFI feed horns can be calibrated to this accuracy using the Crab nebula, while global fits to the sky polarisation should allow us to transfer this calibration to the remaining horns.

Some aspects of the data analysis also require further work. Procedures to correct the maps and power spectra from the distortions introduced by non-ideal beams need to be further developed, and will be needed especially at 44 GHz where the off-diagonal components of the beam Mueller matrices can reach several percent. Correction of intensity-to-polarisation conversion due to bandpass errors remains to be demonstrated. Given the uncertainty in the bandpasses it may even be necessary to derive a basic model of the bandpass from the data. These issues are being addressed in end-to-end testing of the analysis pipeline that are currently ongoing.

Appendix A: Integrated beam response

To obtain the appropriate weighting of different frequencies, it suffices to consider a single-mode antenna observing an unpolarised sky, for which the received power is

$$P = \frac{1}{2}\int_0^\infty \mathrm{d}\nu\, g'(\nu)\, A(\nu) \int_{4\pi} \mathrm{d}\Omega\, \mathcal{B}_I I, \tag{A.1}$$

where A is the effective area of the aperture, Stokes I is measured in intensity units (power per unit frequency per unit solid angle per unit collecting area), and $g'(\nu)$ is a dimensionless gain (Kraus 1966). In general,

$$A(\nu) \int_{4\pi} \mathcal{B}_I(\boldsymbol{n}, \nu)\, \mathrm{d}\Omega = \frac{c^2}{\nu^2}\ \mathrm{sr}. \tag{A.2}$$

Following the convention in the GRASP package (Pontoppidan 2005), we define the beam as a dimensionless gain normalised relative to an ideal isotropic antenna[12]:

$$\int_{4\pi} \mathcal{B}_I\, \mathrm{d}\Omega = 4\pi\ \mathrm{sr}, \tag{A.3}$$

so that $A(\nu) = c^2/4\pi\nu^2$. If we now express Stokes I in terms of Rayleigh-Jeans brightness temperature

$$I(\boldsymbol{n}, \nu) = 2k_B T_B(\boldsymbol{n}, \nu)\, \nu^2/c^2, \tag{A.4}$$

then we have

$$P = \frac{k_B}{4\pi}\int \mathrm{d}\nu\, g'(\nu) \int_{4\pi} \mathrm{d}\Omega\, \mathcal{B}_I T_B. \tag{A.5}$$

If the source fills the beam, then

$$\int_{4\pi} \mathcal{B}_I T_B\, \mathrm{d}\Omega = 4\pi T_B. \tag{A.6}$$

With a top-hat bandpass ($g' = 1$ over bandwidth $\Delta\nu$), and T_B independent of ν we get the familiar

$$P = k_B T_B \Delta\nu. \tag{A.7}$$

Our primary calibration is via the CMB dipole. Considered as a fluctuation against the CMB monopole, its spectrum is the differential of the *Planck* function,

$$\Delta I(\nu) = \left(\frac{\partial B(\nu, T)}{\partial T}\right)_{T_0} \Delta T, \tag{A.8}$$

where ΔT is the amplitude in thermodynamic temperature and

$$\left(\frac{\partial B(\nu, T)}{\partial T}\right)_{T_0} = \frac{2k_B\nu^2}{c^2} \mathrm{e}^{h\nu/k_B T_0} \left(\frac{h\nu/k_B T_0}{\mathrm{e}^{h\nu/k_B T_0} - 1}\right)^2 \tag{A.9}$$

$$\equiv \frac{2k_B\nu^2}{c^2}\eta_{\Delta T}(\nu). \tag{A.10}$$

[12] Hence the beam in dBi is $0.1 \lg \mathcal{B}$.

Thus the power received from the dipole is[13]

$$P = k_B \Delta T \int g'(\nu) \eta_{\Delta T}(\nu)\, \mathrm{d}\nu \tag{A.11}$$

It is convenient to re-normalise the gain so that $k_B g' \equiv G g(\nu)/2$, with G independent of ν, and

$$\int g(\nu) \eta_{\Delta T}(\nu)\, \mathrm{d}\nu = \eta_{\Delta T}(\nu_0), \tag{A.12}$$

where ν_0 is a fiducial frequency whose choice is discussed in Sect. 5.2. Note that G has units $\mathrm{W\,K^{-1}}$.

To take account of polarisation, first assume an ideal OMT with zero cross polarisation, so that

$$\boldsymbol{J}^{\mathrm{amp}} \boldsymbol{J}^{\mathrm{OMT}} = \begin{pmatrix} \sqrt{G_{\mathrm{s}} g_{\mathrm{s}}} & 0 \\ 0 & \sqrt{G_{\mathrm{m}} g_{\mathrm{m}}} \end{pmatrix}. \tag{A.13}$$

Comparing with Eqs. 11 & 12, we see that, for a single detector (one OMT arm),

$$P_i(t) = \frac{G_i(t)}{2} \int_0^\infty \mathrm{d}\nu\, g_i(\nu) \times \frac{1}{4\pi} \int_{4\pi} \mathrm{d}\Omega\, \mathcal{B}^T(\hat{\boldsymbol{n}}, \nu)\, \mathcal{R}(\theta_0)\, \mathcal{S}(\boldsymbol{R}(t)\, \hat{\boldsymbol{n}}) \tag{A.14}$$

where $\mathcal{B}$ is the response Stokes vector constructed from the beam simulation data (so its total-intensity component equals the $\mathcal{B}_I$ that appears in the preceding formulae). The components of the Stokes vector $\mathcal{S}$ must be expressed in terms of brightness temperature. It is apparent that the response vector constructed from $\boldsymbol{J}^{\mathrm{beam}}$ should be $\mathcal{B}/4\pi$.

A non-ideal OMT mixes the response of the two rows of $\boldsymbol{J}^{\mathrm{beam}}$. Nevertheless its response can be put in the form of Eq. (A.14) by multiplying out the Jones matrices, evaluating the net response vector $\mathcal{W}$, and factorising into a scalar gain and Stokes vector beam $\mathcal{B}$ by imposing the normalisation in Eq. (A.3). However, the bandpass functions $g(\nu)$ discussed in the main text do not use this normalisation, but instead represent the co-polar channel only, i.e.

$$\frac{G_i(t)}{2} g_i(\nu) = |J_{ii}^{\mathrm{amp}} J_{ii}^{\mathrm{OMT}}|^2. \tag{A.15}$$

Appendix B: Effects of the bandwidth on the main beam

Because of the variation of response of the feed horns with frequency and the varying ratio of telescope diameter to wavelength, the main beam shape is expected to be frequency dependent within the bandwidth of each detector. Here we present main beam simulations of LFI-27M at frequencies between 27 and 33 GHz; we have also simulated the beam from one RCA in the other two bands and find a very similar behaviour as frequency varies within the band. These computations have been carried out in the same way as the main simulations described in detail by Sandri et al. (2010). The co-polar patterns of the feed horn are shown in Fig. B.1, which also shows two relevant angles: the angle subtended by the lower part of the subreflector[14], and the angle beyond which all rays coming from the feed hitting the subreflector fall in the main spillover region. Obviously, these two angles depend on the plane considered: in Fig. B.1 only the E-plane is presented ($\phi = 90°$ in the feed horn coordinate system, because the feed is Y-polarised). Figure B.2 reports the corresponding taper at 22° computed in the E-plane, in the H-plane, and in the 45° plane. It is noteworthy that the nominal edge taper for this horn, (30 dB at 22°, see Sandri et al. (2010)), is reached only in the E-plane and that the equalisation of the edge taper on these three planes is at about 32.5 GHz. In other words, the maximum pattern symmetry, that corresponds to the minimum level of cross-polarisation, is reached at this frequency and not at the central frequency. This is due to the fact that the horn has been designed taking into account the edge taper requirement on the E-plane at 30 GHz and no requirement on the pattern equalisation was imposed.

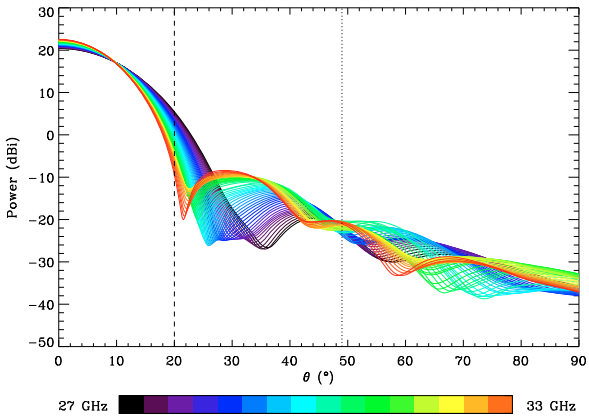

Fig. B.1. Profiles of the E-plane co-polar pattern of the 30 GHz feed horn LFI-27M, at 0.1 GHz intervals between 27 and 33 GHz. Two relevant angles are shown: the angle subtended by the lower part of the subreflector (vertical dotted line at about 49° from the feed boresight direction) and the angle beyond which all rays coming from the feed hitting the subreflector fall in the main spillover region (vertical dashed line at about 20° from the feed boresight direction). Of course, these two angles depend on the plane considered and the values reported here are those in the E-plane.

A direct consequence of the edge taper variation with frequency is that the mirrors are less illuminated at higher frequency. This effect compensates for the fact that the mirror diameter at higher frequency is greater in terms of wavelength, leading to an almost-constant beamwidth across the band, as shown in Fig. B.3. It is evident from this and subsequent figures that the bandwidth effect on the main beams is not analytically predictable, and instead must be studied via simulations like those presented here. From Fig. B.3 it can be inferred that the beam geometry is hardly changed at least up to −20 dB from the power peak, because the full widths at −3, −10, and −20 dB do not change significantly within the bandwidth. The full patterns at the nominal band edges and averaged over the band are shown in Fig. B.4.

Some relevant main beam characteristics are reported in Table B.1 and shown in Fig. B.5. From these figures it should be noted that: i) the beam directivity varies little (total change of about 0.5%) across the band, despite a 10.4% variation in feed directivity, due to the compensation effect described above; ii) the cross polar discrimination factor, XPD, (ratio of peak cross-polar to peak co-polar power response) is always at least

[13] Here we ignore the contribution of the far sidelobes, see e.g. Burigana et al. (2006).

[14] In fact, with respect to the feed horn coordinate system, the lower part of the subreflector is at negative θ values, but the feed horn pattern is symmetric.

Table B.1. Main beam characteristics as a function of frequency for the 30 GHz channel, for the *Y*-polarisation (main arm) of feed horn LFI-27.

Frequency (GHz)	Edge Taper (dB @ 22°)	$\mathcal{D}_{\rm feed}{}^a$ (dBi)	*FWHM* (arcmin)	e^b	τ^c (°)	$\mathcal{D}^d$ (dBi)	XPD^e (dB)	d^f (%)	$\mathcal{S}^g$ (%)
27.0	18.59	20.42	32.80	1.32	−89.9	51.06	27.09	0.556	0.87
27.2	19.11	20.51	32.80	1.32	−89.9	51.06	27.19	0.542	0.80
27.4	19.64	20.59	32.75	1.32	−89.9	51.08	27.26	0.531	0.75
27.6	20.18	20.67	32.74	1.33	−89.9	51.09	27.30	0.521	0.71
27.8	20.74	20.75	32.72	1.34	−89.9	51.10	27.38	0.510	0.66
28.0	21.33	20.84	32.72	1.34	−89.9	51.10	27.47	0.498	0.62
28.2	21.97	20.93	32.66	1.35	−90.0	51.10	27.56	0.487	0.59
28.4	22.65	21.01	32.73	1.36	−90.0	51.10	27.61	0.477	0.56
28.6	23.40	21.09	32.77	1.36	−90.0	51.09	27.68	0.467	0.55
28.8	24.21	21.17	32.80	1.37	−90.0	51.08	27.80	0.457	0.53
29.0	25.08	21.25	32.91	1.38	90.0	51.08	27.95	0.447	0.53
29.2	26.01	21.34	32.98	1.38	90.0	51.06	28.10	0.437	0.53
29.4	27.04	21.42	33.05	1.39	90.0	51.04	28.19	0.430	0.53
29.6	28.19	21.51	33.08	1.40	90.0	51.03	28.28	0.424	0.54
29.8	29.35	21.59	33.15	1.40	90.0	51.01	28.41	0.418	0.55
30.0	30.43	21.67	33.23	1.41	89.9	51.00	28.31	0.412	0.58
30.2	31.52	21.74	33.35	1.41	89.9	50.98	28.20	0.405	0.62
30.4	32.74	21.80	33.42	1.41	89.9	50.95	28.17	0.399	0.65
30.6	33.80	21.88	33.50	1.41	89.9	50.93	28.18	0.393	0.67
30.8	34.56	21.96	33.58	1.42	89.9	50.92	28.13	0.388	0.69
31.0	34.77	22.03	33.63	1.41	89.9	50.91	28.01	0.384	0.73
31.2	34.57	22.10	33.63	1.41	89.9	50.90	27.96	0.379	0.77
31.4	34.40	22.16	33.70	1.40	89.9	50.89	28.04	0.371	0.79
31.6	34.42	22.22	33.70	1.40	89.9	50.89	28.30	0.363	0.80
31.8	34.46	22.27	33.66	1.40	90.0	50.89	28.58	0.356	0.80
32.0	34.57	22.31	33.62	1.39	90.0	50.89	28.88	0.349	0.80
32.2	35.12	22.36	33.62	1.39	−90.0	50.90	29.20	0.343	0.80
32.4	36.44	22.41	33.62	1.39	−90.0	50.90	29.38	0.341	0.80
32.6	38.60	22.45	33.68	1.41	−89.9	50.90	29.07	0.342	0.79
32.8	40.77	22.49	33.80	1.42	−89.9	50.88	28.63	0.347	0.78
33.0	41.00	22.54	34.02	1.44	−89.9	50.86	28.36	0.350	0.79

Notes. [a] feed directivity; [b] ellipticity; [c] rotation angle of the polarisation ellipse; [d] main beam directivity; [e] cross polar discrimination factor; [f] main beam depolarisation parameter; [g] spillover.

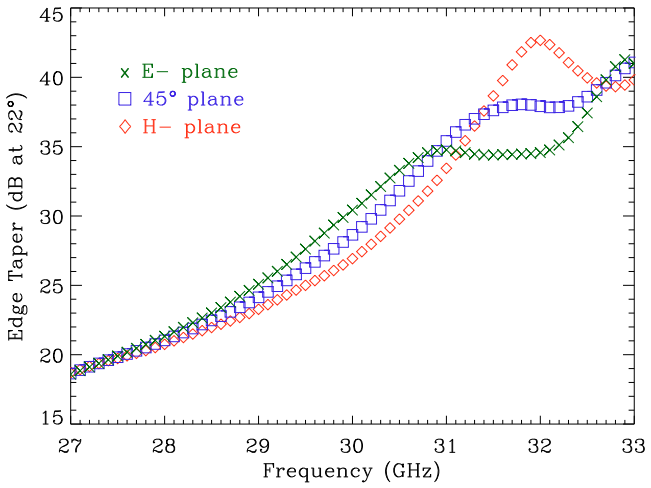

Fig. B.2. Feed horn taper at 22°(corresponding approximately to the edge of the primary mirror) versus frequency.

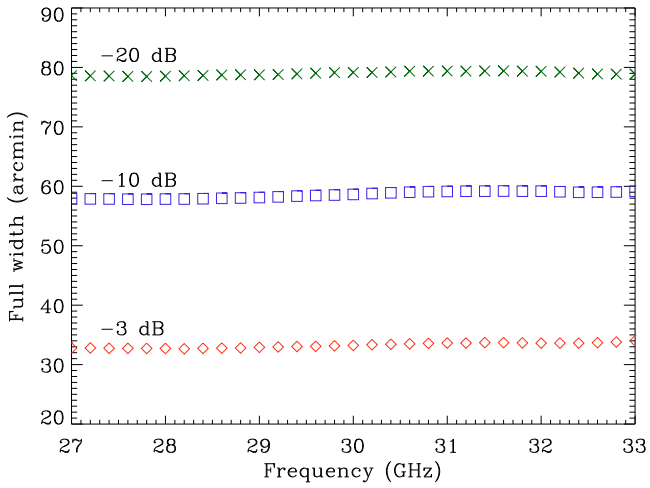

Fig. B.3. Full width at −3, −10, and −20 dB from the main beam power peak. No significant trend with the frequency is evident from these curves.

25 dB, within the specification; iii) a spread of about 6% is evident in the FWHM, following the trend of the edge taper value; iv) the spillover initially decreases because the main lobe gets narrower, then it increases due to the growth of the first sidelobe up to 10 dB higher, and finally, between 32 and 33 GHz it

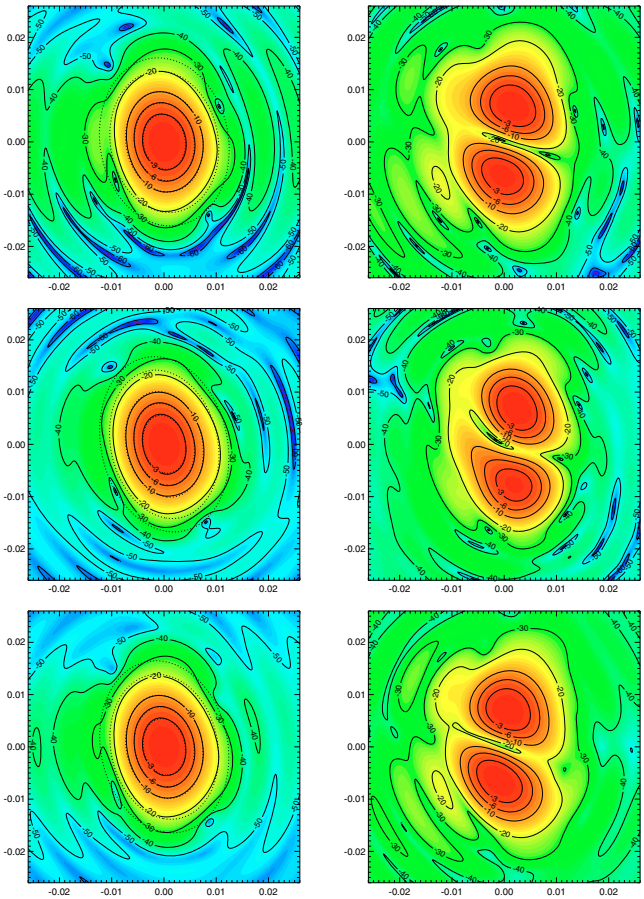

Fig. B.4. Main beam at 27 GHz (*first row*), 33 GHz (*second row*), and averaged main beam over the nominal 27–33 GHz bandpass. (*third row*). Co-polar pattern is on the left side and cross-polar pattern is on the right side. Colour scale goes from −90 to 0 dB. Contours (dotted) of a fitted bivariate Gaussian are superimposed; the fitted averaged FWHM are 32.09, 33.10, and 32.53 arcmin, respectively.

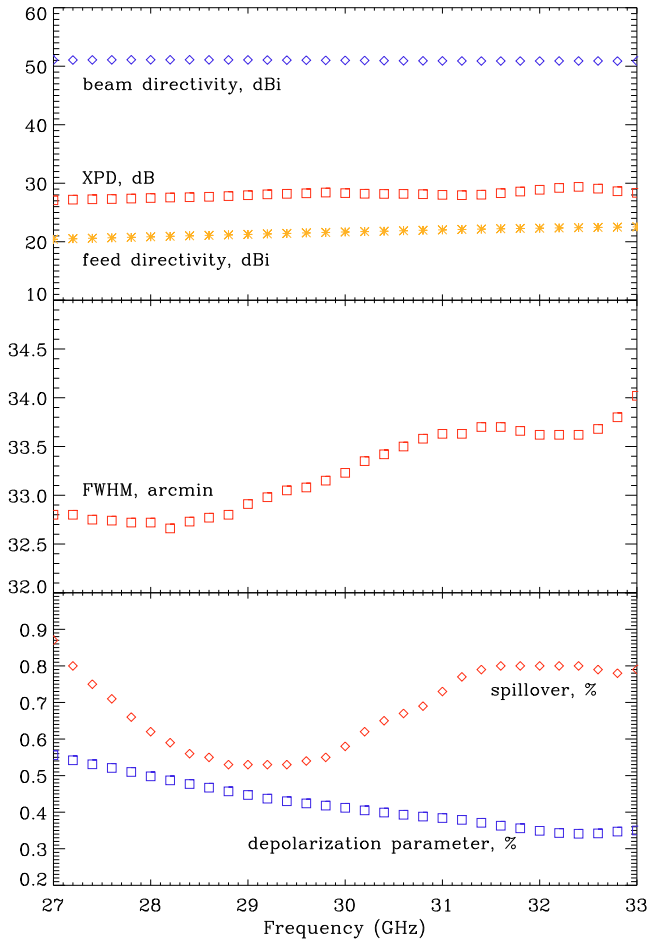

Fig. B.5. Feed horn directivity, main beam directivity, and XPD (*top panel*), FWHM (*central panel*), spillover and depolarisation parameter (*bottom panel*).

decreases again because the sidelobe gets narrower and the first minimum become more evident; *v*) the beam depolarisation[15] decreases with frequency.

The effective band-averaged beam will be weighted by the bandpass and the brightness spectrum, whereas uniform weights have been used for the patterns analysed here. Weighted-average beams will be used for the final analysis but are not available for this pre-launch analysis since the time-consuming physical-optics simulations required have only been completed for one polarisation of one horn in each band, and only within the nominal passband whereas the actual response is significant over a wider frequency range, as shown by Zonca et al. (2009). The results presented here suffice to show that beamshape variation across the band is a second-order effect, and therefore justifies our separation of bandpass and beam effects on the polarisation in the main text.

[15] Defined as in Sandri et al. (2010); in our notation, $d = 1 - \sqrt{\langle W_Q\rangle^2 + \langle W_U\rangle^2 + \langle W_V\rangle^2}/\langle W_I\rangle$.

Acknowledgements. J.P.L. thanks Johan Hamaker for a fruitful collaboration (Hamaker & Leahy 2004) which has significantly influenced the presentation in this paper. J.P.L. also thanks the Osservatorio Astronomico di Trieste for hospitality while much of this paper was written. We thank the referee for a perceptive review. The *Planck*-LFI project is developed by an International Consortium led by Italy and involving Canada, Finland, Germany, Norway, Spain, Switzerland, UK, USA. The Italian contribution to *Planck* is supported by the Italian Space Agency (ASI). The UK contribution is supported by the Science and Technology Facilities Council (STFC). The Finnish contribution is supported by the Finnish Funding Agency for Technology and Innovation (Tekes) and the Academy of Finland. The Canadian contribution is supported by the Canadian Space Agency. We wish to thank people of the *Herschel*/*Planck* Project of ESA, ASI, THALES Alenia Space Industries, and the LFI Consortium that are involved in activities related to optical simulations and the measurement and modelling of the radiometer performance. We acknowledge the use of the *Planck* sky model, developed by the Component Separation Working Group (WG2) of the *Planck* Collaboration. We thank the members of the *Planck* CTP working group for the preparation and validation of the Trieste simulations. Some of the results in this paper have been derived using the HEALPix (Gorski et al. 1999). We acknowledge the use of the Legacy Archive for Microwave Background Data Analysis (LAMBDA). Support for LAMBDA is provided by the NASA Office of Space Science. This research has made use of NASA's Astrophysics Data System. We acknowledge partial support of the NASA LTSA Grant NNG04CG90G.

References

Armitage-Caplan, C., & Wandelt, B. D. 2009, ApJS, 181, 533
Ashdown, M. A. J., Baccigalupi, C., Balbi, A., et al. 2007, A&A, 471, 361
Ashdown, M. A. J., Baccigalupi, C., Bartlett, J. G., et al. 2009, A&A, 493, 753
Battaglia, P., Francheschet, C., Zonca, A., et al. 2009, JINST, 4, T12014
Berkhuijsen, E. M. 1975, A&A, 40, 311
Bersanelli, M., Mandolesi, N., Butler, R. C., et al. 2010, A&A, 520, A4
Bietenholz, M. F., & Kronberg, P. P. 1991, ApJ, 368, 231

Bond, J. R., Jaffe, A. H., & Knox, L. 1998, PRD, 57, 2117
Burigana, C., Gruppuso, A., & Finelli, F. 2006, MNRAS, 371, 1570
Cappellini, B., Maino, D., Albetti, G., et al. 2003, A&A, 409, 375
D'Arcangelo, O., Figini, L., Simonetto, A., et al. 2009a, JINST, 4, T12007
D'Arcangelo, O., Simonetto, A., Figini, L., et al. 2009b, JINST, 4, T12005
Davis, R. J., Wilkinson, A., Davies, R. D., et al. 2009, JINST, 4, T12002
Draine, B. T., & Lazarian, A. 1998, ApJ, 494, L19
Eriksen, H. K., Jewell, J. B., Dickinson, C., et al. 2008, ApJ, 676, 10
Gorski, K. M., Wandelt, B. D., Hansen, F. K., Hivon, E., & Banday, A. J. 1999, unpublished [arXiv:astro-ph/9905275]
Green, D. A., Tuffs, R. J., & Popescu, C. C. 2004, MNRAS, 355, 1315
Hamaker, J. P. 2000, A&AS, 143, 515
Hamaker, J. P., & Bregman, J. D. 1996, A&AS, 117, 161
Hamaker, J. P., & Leahy, J. P. 2004, A study of CMB differencing polarimetry with particular reference to *Planck*, Tech. Rep. SCI-A/2003.312/JT, ESA
Hamaker, J. P., Bregman, J. D., & Sault, R. J. 1996, A&AS, 117, 137
Heeschen, D. S., & Howard, W. E. 1974, in Trans. IAU, Vol. XVB, Proc. 1973 General Assembly, ed. G. Contoupoulos & A. Jappel (Dordrecht: Reidel), 165
Hinshaw, G., Weiland, J. L., Hill, R. S., et al. 2009, ApJS, 180, 225
Hu, W., & Dodelson, S. 2002, ARA&A, 40, 171
Hu, W., Hedman, M. M., & Zaldarriaga, M. 2003, PRD, 67, 043004
Jarosik, N., Barnes, C., Greason, M. R., et al. 2007, ApJS, 170, 263
Jones, W. C., Montroy, T. E., Crill, B. P., et al. 2007, A&A, 470, 771
Keihänen, E., Kurki-Suonio, H., & Poutanen, T. 2005, MNRAS, 360, 390
Keihänen, E., Keskitalo, R., Kurki-Suonio, H., Poutanen, T., & Sirvio, A.-S. 2010, A&A, 510, 57
Kogut, A., Dunkley, J., Bennett, C. L., et al. 2007, ApJ, 665, 355
Kraus, J. D. 1966, Radio Astronomy (New York: McGraw-Hill)
Kurki-Suonio, H., Keihänen, E., Keskitalo, R., et al. 2009, A&A, 506, 1511
Lamarre, J.-M., Puget, J.-L., Ade, P. A. R., et al. 2010, A&A, 520, A9
Leahy, J. P., & Foley, K. 2006, Proc.Science, PoS(CMB2006), 043
Ludwig, A. C. 1973, IEEE Trans.-AP, 21, 116
Mandolesi, N., Bersanelli, M., Butler, R. C., et al. 2010, A&A, 520, A3
Meinhold, P., Leonardi, R., Aja, B., et al. 2009, JINST, 4, T12009
Mennella, A., Bersanelli, M., Seiffert, M., et al. 2003, A&A, 410, 1089
Mennella, A., Bersanelli, M., Butler, R. C., et al. 2010, A&A, 520, A5
Morgante, G., Pearson, D., Melot, F., et al. 2009, JINST, 4, T12016
Netterfield, C. B., Ade, P. A. R., Bock, J. J., et al. 2002, ApJ, 571, 604
O'Dea, D., Challinor, A., & Johnson, B. R. 2007, MNRAS, 376, 1767
Page, L., Hinshaw, G., Komatsu, E., et al. 2007, ApJS, 170, 335
Perley, R. A. 1982, AJ, 87, 859
Pontoppidan, K. (ed.) 2005, GRASP9 Technical Description (Copenhagen: TICRA Engineering Consultants)
Rosset, C., Yurchenko, V. B., Delabrouille, J., et al. 2007, A&A, 464, 405
Sandri, M., Villa, F., Bersanelli, M., et al. 2010, A&A, 520, A7
Seiffert, M., Mennella, A., Burigana, C., et al. 2002, A&A, 391, 1185
Tauber, J. A., Mandolesi, N., Puget, J.-L., et al. 2010a, A&A, 520, A1
Tauber, J. A., Norgaard-Nielsen, H. U., Ade, P. A. R., et al. 2010b, A&A, 520, A2
Tinbergen, J. 1996, Astronomical Polarimetry (Cambridge University Press)
Valenziano, L., Cuttaia, F., De Rosa, A., et al. 2009, JINST, 4, T12006
Villa, F., D'Arcangelo, O., Pecora, M., et al. 2009, JINST, 4, T12004
Zaldarriaga, M. & Seljak, U. 1997, PRD, 55, 1830
Zonca, A., Franceschet, C., Battaglia, P., et al. 2009, JINST, 4, T12010

[1] Jodrell Bank Centre for Astrophysics, School of Physics and Astronomy, University of Manchester, M13 9PL, UK
e-mail: j.p.leahy@manchester.ac.uk
[2] Osservatorio Astronomico di Trieste - INAF, via Tiepolo 11, 34143 Trieste, Italy
[3] Università degli Studi di Milano, Dipartimento di Fisica, Italy
[4] IASF - Sezione di Milano, INAF, Milano, Italy
[5] Istituto di Fisica del Plasma - CNR, via Cozzi 53, 20125 Milano, Italy
[6] Laboratoire APC/CNRS, Bâtiment Condorcet, 10 rue Alice Domon et Léonie Duquet, 75205 Paris Cedex 13, France
[7] SISSA/ISAS, Astrophysics Sector, via Beirut 2-4, Sezione di Trieste, 34014 Trieste, Italy
[8] INFN, Sezione di Trieste, 34014 Trieste, Italy
[9] Department of Physics & Astronomy, University of British Columbia, Vancouver, BC, V6T 1Z1 Canada
[10] Department of Physics, University of Helsinki, PO Box 64, 00014 Helsinki, Finland
[11] Helsinki Institute of Physics, PO Box 64, 00014 Helsinki, Finland
[12] Metsähovi Radio Observatory, TKK, Helsinki University of Technology, Metsähovintie 114, 02540 Kylmälä, Finland
[13] Istituto di Astrofisica Spaziale e Fisica Cosmica - Sezione di Bologna, INAF, Bologna, Italy
[14] European Space Agency (ESA), Astrophysics Division, Keplerlann 1, 2201 AZ, Noordwijk, The Netherlands
[15] INAF - Trieste, 34131 Trieste, Italy
[16] Computational Cosmology Center, Lawrence Berkeley National Laboratory, Berkeley, CA 94720, USA
[17] Space Sciences Laboratory, University of California Berkeley, Berkeley CA 94720, USA
[18] Dipartimento di Fisica, Università degli Studi di Trieste, Italy
[19] Department of Physics, University of California, Santa Barbara, CA 931106, USA
[20] Planck Science Office, European Space Agency, European Space Astronomy Centre, PO Box – Apdo. de correos 78, 28691 Villanueva da la Caada, Madrid, Spain
[21] Jet Propulsion Laboratory, California Institute of Technology, Pasadena, CA 91109, USA
[22] Department of Physics, California Institute of Technology, Pasadena, CA 91125, USA